JOURNAL OF COMPUTATIONAL PHYSICS 64, 279–319 (1986)

Vortex Dynamics of Cavity Flows*

K. GUSTAFSON

Department of Mathematics, University of Colorado, Boulder, Colorado 80309

AND

K. HALASI

Department of Mathematics, University of Louisville, Louisville, Kentucky 40292

Received February 6, 1985; revised May 31, 1985

The unsteady viscous incompressible Navier–Stokes flow in a driven cavity is studied with particular attention to the formation and evolution of vortices and eddies. These are compared in the limit to previous steady flow simulations. Results include new details of the dynamics of secondary eddy separation and subsequent coalescence into subprimary vortices, and the fine structure of deep cavity flow. Enhanced flow topography is obtained by means of pressure and kinetic energy portraits.

1. INTRODUCTION

Flow in a rectangular cavity with the motion driven by the uniform translation of the top lid occupies a position of considerable theoretical significance within the larger class of separated flows. Below in Table I may be found a brief summary of some of the important representative studies. There are many others, most of which may be found from the references of the studies cited in Table I.

Early numerical simulations of two-dimensional Navier–Stokes flows within a cavity tended to focus on the ambulatory nature, with respect to Reynolds numbers, of the primary vortex in a steady flow. In particular, in an early paper Kawaguti [13] experimented for a small range ($Re < 64$) of Reynolds numbers in cavities both deep and shallow. His observations included the downstream drift w.r.t. Reynolds number of the primary vortex center, in addition to the formation of corner eddies in the deep cavities. By 1966 Burggraf [5] had shown that the numerical integration of the steady Navier–Stokes equations for a square cavity yielded a large primary vortex near the center of the cavity, along with two secon-

* Partially supported by NSF Grant MCS 80-12220, and by a grant of computing resources NCAR Grant 35071080.

0021-9991/86 $3.00

TABLE I

Representative Cavity Flow Studies

Study	Flow	Formulation, Method
Kawaguti [13] (1961)	Steady, linear	Stream function, vorticity; Finite difference method
Moffatt [14] (1964)	Steady, linear	Stream function, theoretical; Similarity solutions
Burggraf [5] (1966)	Steady, linear	Stream function, vorticity; Relaxation
Pan and Acrivos [5] (1967)	Steady, linear	Stream function, experimental; Relaxation, localization
Bozeman and Dalton [4] (1973)	Steady, nonlinear	Stream function, vorticity; Implicit finite differences
Benjamin and Denny [3] (1979)	Steady, nonlinear	Stream function, vorticity; False transients
Gatski, Grosch, and Rose [6] (1982)	Unsteady, nonlinear	Velocity, voticity; Compact finite differences
Ghia, Ghia, and Shin [7] (1982)	Steady, nonlinear	Stream function, vorticity; Multigrid, fine mesh
Schreiber and Keller [17, 18] (1983)	Steady, nonlinear	Stream function, vorticity; Newton, continuation
Agarwal [1] (1984)	Steady, nonlinear	Stream function, vorticity; Third order, upwind differencing

dary eddies near the bottom corners. This was shown for a range of Re between 0 and 400. Subsequent works of Benjamin and Denny [3], Ghia, Ghia, and Shin [7], Schreiber and Keller [17, 18], and Agarwal [1] revealed tertiary corner eddies for large Reynolds numbers.

Pan and Acrivos [15] produced experimental results for a range of rectangular sites. More recent visualizations of the cavity problem (Taneda [19], see also Van Dyke [21]) exhibited separating stream lines for a range of geometric configurations. The existence of a sequence of eddies of decreasing relative strengths was shown to occur near sharp corners, corresponding to the theoretical investigations of Moffat [14] on Stokes flows. For a recent survey of corner eddy theory for steady Stokes flow, including the effect of mass injection, see Jeffrey and Sherwood [12]. See also Gustafson and Leben [11] for a comparative multigrid study of finer corner eddies of steady flow.

As may be noted from Table I and the above discussion, the preponderance of studies to date have dealt with the steady formulation of the problem, and most used the stream function, vorticity variables. Our first goal was to implement a study of the full unsteady problem in the primitive variables pressure and velocity with emphasis on the dynamic development of corner vortices especially as dependent on Reynolds number and cavity aspect ratio. A second goal was to time march the full unsteady equations to a "steady state" in cavities of various depths and for

different Reynolds numbers for comparison to the previous steady flow calculations. A third goal was to examine the interaction between Reynolds number and nonlinearlity. Overall, we wished to generate extensive new portraits of the evolving vortex dynamics. In all of the figures presented in this paper, the velocity and pressure gradients were normalized by dividing by their magnitudes, to emphasize the qualitative development.

2. Numerical Formulation and Basic Results

The recent appearance of the excellent treatments by Peyret and Taylor [16], see also Thomasset [20], especially for finite element methods, provides adequate detailed discussions of the cavity flow problem. See also the papers referenced in Table I.

2.1. *Some Preliminary Clarifications*

We will always consider a two-dimensional cavity with lid under uniform translation to the left as shown in Fig. 1. Results typical of our flow portraits, to the elaborated upon in this paper, are shown in Fig. 2.

There are several variations on this basic problem which should now be mentioned. First, some studies move the lid to the right. Second, some studies have smoothed the singularities at the lid corners, e.g., as is done in Peyret and Taylor [16]. This appears to have negligible effect on the internal and lower qualitative features of separation and eddy formation. Third, there is the driving of the cavity by a continuous fluid rather than lid travelling over the top of the cavity. Although this causes a slight downward pressure on the streamlines near the top of the cavity, e.g., see Azmy and Dorning [2], so long as the fluid densities are not different it appears to produce no dramatically different effects either in the simulation or in physical experiments (Taneda [19]; see also Van Dyke [21]).

2.2. *Primitive Variable Scheme*

The viscous incompressible Navier–Stokes equations

$$V_t - \frac{1}{Re}\Delta V + (V\cdot\nabla)V = -\nabla p \tag{2.1}$$

$$\nabla\cdot V = 0 \tag{2.2}$$

in the cavity were discretized on a uniform grid using a MAC (marker and cell) scheme. The initial condition of the cavity problem is characterized by an everywhere zero velocity field, except for the top layer which is moving to the left at unit velocity.

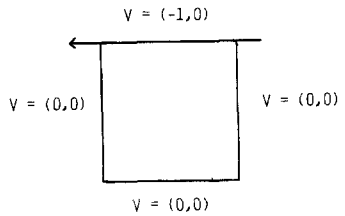

FIG. 1. Driven cavity, aspect ratio $A = 1$.

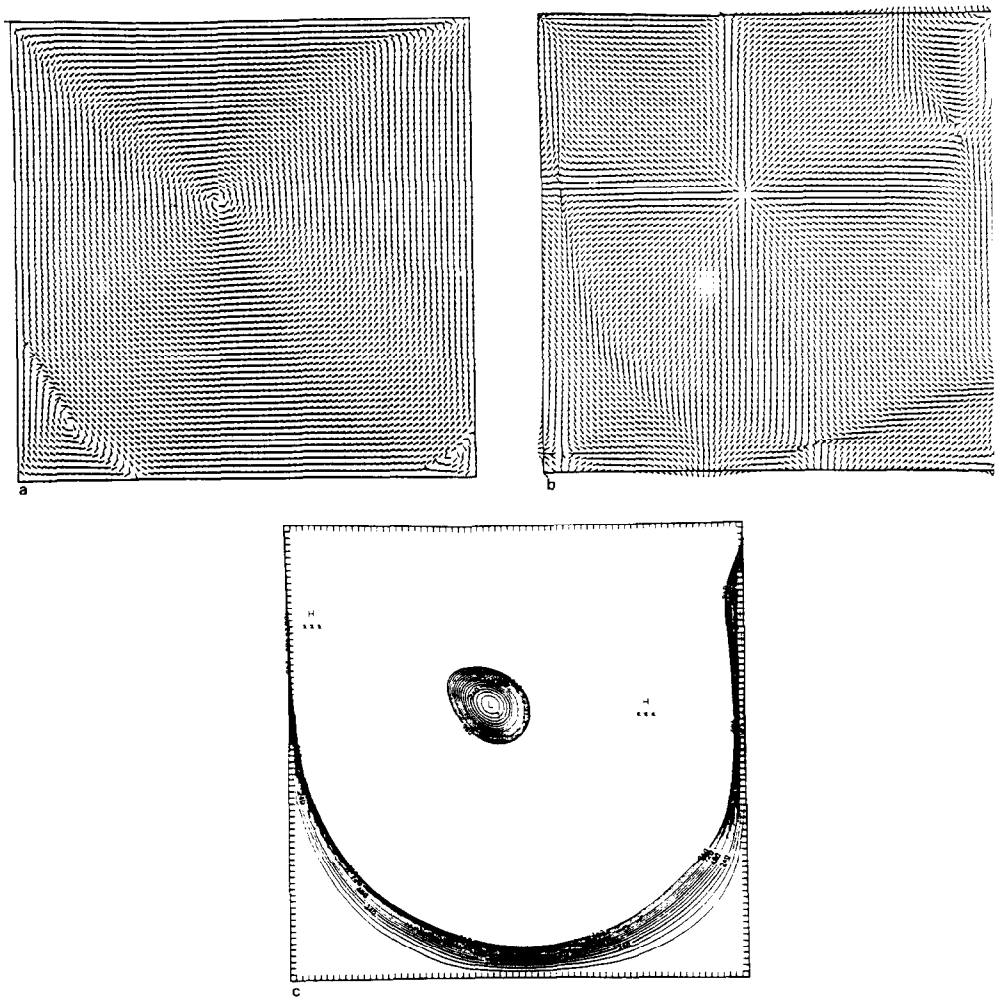

FIG. 2. Typical flow portraits. Reynolds number $\mathrm{Re} = 400$, aspect ratio $A = D/W = 1$, time $t = 25.5$ S, flow is almost steady. Velocity and pressure gradient amplitudes are noramlized to better reveal the qualitative features of simulated flow. The kinetic energy contours shown here lie within the window from 0.00 to approximately 0.01, with labels scaled by $0.1E+06$. (a) Velocity. (b) Pressure gradient. (c) Kinetic energy.

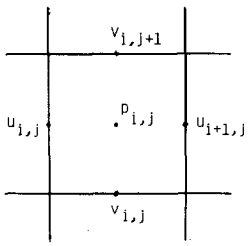

FIG. 3. Computational cell and variable loci assignments.

The two-dimensional version of Eqs. (2.1) and (2.2) expressed in conservative form in terms of the individual components is given by

$$u_t + (u^2)_x + (uv)_y = -p_x + \frac{1}{Re}(u_{xx} + u_{yy}) \tag{2.3}$$

$$v_t + (uv)_x + (v^2)_y = -p_y + \frac{1}{Re}(v_{xx} + v_{yy}) \tag{2.4}$$

$$u_x + v_y = 0. \tag{2.5}$$

In the MAC discretization scheme we construct N computational cells in the x-direction and M computational cells in the y-direction. The pressure value $p_{i,j}$ for the $i-j$th cell is kept at the center of that cell. The midpoints of the left and right vertical boundaries of each cell are used for the x-directional velocity component u, while the midpoints of the horizontal boundaries are used as sites for the y-directional velocity component v. In this way we obtain an $(N+1)\times M$ array of u values, an $(M+1)\times N$ array of v values, and an $N\times M$ array of pressure values p. The assignment of these loci is shown in Fig. 3. For the sake of simplicity, let $FU^n_{i+1,j}$ and $FV^n_{i,j+1}$ represent the finite differencing of the combined advection and viscous terms $-(u^2)_x-(uv)_y+(1/Re)(u_{xx}+u_{yy})$ and $-(uv)_x-(v^2)_y+(1/\mathrm{Re})(v_{xx}+v_{yy})$, respectively, at the nth time step. Then in the MAC scheme we have

$$FU^n_{i+1,j} = \frac{[\frac{1}{2}(u_{i,j}+u_{i+1,j})]^2 - [\frac{1}{2}(u_{i+1,j}+u_{i+2,j})]^2}{\delta x} + \frac{\frac{1}{4}(u_{i+1,j}+u_{i+1,j-1})(v_{i,j}+v_{i+1,j}) - \frac{1}{4}(u_{i+1,j}+u_{i+1,j+1})(v_{i,j+1}+v_{i+1,j+1})}{\delta y} + \frac{1}{Re}\left[\frac{(u_{i+2,j}+u_{i,j}-2u_{i+1,j})}{\delta x^2} + \frac{(u_{i+1,j+1}+u_{i+1,j-1}-2u_{i+1,j})}{\delta y^2}\right] \tag{2.6}$$

$$FV^n_{i,j+1} = \frac{\frac{1}{4}(u_{i,j}+u_{i,j+1})(v_{i-1,j+1}+v_{i,j+1}) - \frac{1}{4}(u_{i+1,j}+u_{i+1,j+1})(v_{i,j+1}+v_{i+1,j-1})}{\delta x}$$
$$+ \frac{[\frac{1}{2}(v_{i,j}+v_{i,j+1})]^2 - [\frac{1}{2}(v_{i,j+1}+v_{i,j+2})]^2}{\delta y}$$
$$+ \frac{1}{Re}\left[\frac{(v_{i+1,j+1}+v_{i-1,j+1}-2v_{i,j+1})}{\delta x^2} + \frac{(v_{i,j+2}+v_{i,j}-2v_{i,j+1})}{\delta y^2}\right], \tag{2.7}$$

where δx and δy denote the dimensions of the cell. It is to be understood that all velocity values correspond to time $t = n\Delta t$.

The full finite difference form of Eqs. (2.3) and (2.4) becomes

$$\frac{u^{n+1}_{i+1,j} - u^n_{i+1,j}}{\Delta t} = FU^n_{i+1,j} + \frac{p^{n+1}_{i,j} - p^{n+1}_{i+1,j}}{\delta x} \tag{2.8}$$

and

$$\frac{v^{n+1}_{i,j+1} - v^n_{i,j+1}}{\Delta t} = FV^n_{i,j+1} + \frac{p^{n+1}_{i,j} - p^{n+1}_{i,j+1}}{\delta y} \tag{2.9}$$

while the compressibility condition, Eq. (2.5), has for its discrete version

$$\frac{u_{i+1,j} - u_{i,j}}{\delta x} + \frac{v_{i,j+1} - v_{i,j}}{\delta y} = 0. \tag{2.10}$$

The latter necessitates the introduction of fictitious computation cells. The velocity values at the fictitious nodes must be assigned not only to enforce the non-slip boundary condition but also must supply a compatible boundary condition for the pressure equation. To approximate the no-slip condition at the walls of the cavity, we require that the velocity values at the fictious nodes just outside the walls be of same magnitude, but of opposite sign, as their corresponding virtual images inside the boundary walls. The impermeable condition of the flow needs no recourse to the fictitious points outside the cavity, since, by nature of the mesh system employed, this condition is met as a boundary constraint.

The fact that on the MAC grid one has $L = DG$, where L, D, G are the discrete Laplacian, divergence, and gradient, is important and allows us the use of fast direct Poisson solvers to calculate efficiently at each time step the adjusting pressure field. Our choice of a solver came from the NCAR FISHPACK Library. The use of iterative methods for many time steps (e.g., $O(10^4)$) Poisson inversions would be prohibitive. The forward Euler marching scheme was chosen for its simplicity of formulation and execution. In advancing the pressure, we chose not to skip any time steps although in retrospect our studies indicate that this practice does not seem to significantly affect the dynamic evolution of the flow and therefore could be recommended when computing resources are limited. We also implemented an implicit method (built upon the trapezoid rule) which yielded very similar results.

The implicit scheme displayed no advantages over the forward Euler scheme. Its capability to allow for a larger time step was opposed by the necessity of inverting two Poisson equations.

Criteria in choosing the time step increment Δt were taken, in part, from the standard constraints for models of diffusion-transport systems, and were augmented by empirical data. For example, the diffusion condition that, for the case in which $\delta_x = \delta y$, the ratio $4\delta t/Re\,\delta x^2$ not exceed some critical value $K(Re) < 1$ necessitates experimental knowledge about the Reynolds number in question in order to gain a priori approximations to $K(Re)$. This knowledge was usually gained by running the flows on coarse grids.

2.3. *Incompressibility*

2.3.1. *Pressure Boundary Conditions*

As indicated above, condition (2.2) is applied to (2.1) to yield the continuous pressure equations

$$-\Delta p = \nabla \cdot [(V \cdot \nabla)\, V]. \tag{2.11}$$

In discretized form the forward Euler marching scheme of the MAC method first advances in time the advection-diffusion component of the flow

$$\tilde{V}^{n+1} = V^n + \Delta t F(V^n), \tag{2.12}$$

where $F(V^n)$ denotes $-(V^n \cdot G)\, V^n + (1/Re)\, L(V^n)$, and V^n is the velocity vector at time step n. The pressure field is then readjusted according to

$$DG(p^{n+1}) = (\Delta t)^{-1}\, D(\tilde{V}^{n+1}), \tag{2.13}$$

ensuring conservation of matter at the next time step, i.e., $D(V^{n+1}) = 0$.

In Fig. 4 we assume zero divergence for the cell inside the cavity, and require that the divergence of the adjacent, outside cell also vanish. The third fictitious velocity value u', heretofore undefined, may then be determined. In general, its value will be that of its virtual image u inside the cavity wall. Then application of the momentum equation (2.8) at the wall yields the Neumann boundary data for the pressure $p' =$

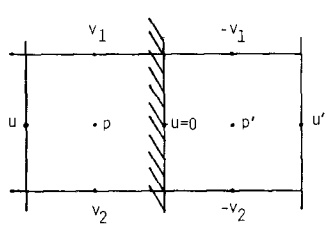

FIG. 4. Assignment of velocity and pressure values at fictitious nodes of right boundary wall.

$p + (2u)/(\delta x Re)$. Similar results are obtained for the remaining possible configurations.

2.3.2. *Velocity Boundary Conditions and Helmholtz Decomposition*

As concerns the effect of the velocity boundary condition on incompressibility, and somewhat related to the discussion of boundary conditions in Gatski *et al.* [6], we would like to make here a general observation (see Gustafson and Halasi [10]).

Consider the Helmholtz decomposition of the intermediate velocity field $\tilde{V}^{n+1}$, as defined in Eq. (2.12), according to

$$\tilde{V}^{n+1} = \tilde{V}_1^{n+1} + \tilde{V}_2^{n+1} + \tilde{V}_3^{n+1}, \tag{2.14}$$

where $\tilde{V}_1^{n+1}$ and $\tilde{V}_2^{n+1}$ are the curl-free and divergence-free components of $\tilde{V}^{n+1}$, respectively. The third component $\tilde{V}_3^{n+1}$ is both curl-free and divergence-free. To obtain the desired incompressible flow vector V^{n+1} a conservative force field, such as pressure gradient, is introduced. Thus $V^{n+1} = \tilde{V}^{n+1} - \nabla(p^{n+1})\,\Delta t$, and the vorticity is left unaffected. The three velocity fields defined by $W_1^{n+1} = \tilde{V}^{n+1} - \tilde{V}_1^{n+1}$, $W_2^{n+1} = \tilde{V}^{n+1} - \tilde{V}_1^{n+1} - \tilde{V}_3^{n+1}$, and $V^{n+1} = \tilde{V}^{n+1} - \nabla(p^{n+1})\,\Delta t$ all have the same vorticity, and all are divergence-free.

This apparent dilemma of nonuniqueness is resolved by first considering the irrotational components of flow. Being curl-free, the component $\tilde{V}_1^{n+1}$ is therefore expressible as the gradient of some scalar field S, $\tilde{V}_1^{n+1} = \nabla S$, from which we obtain

$$\nabla^2 S = \nabla \cdot (\tilde{V}_1^{n+1}) = \Delta t \nabla^2 p.$$

The Newmann boundary condition for S is

$$\left.\frac{\partial S}{\partial n}\right|_{\partial\Omega} = n \cdot \tilde{V}_1^{n+1}|_{\partial\Omega}.$$

For general domains it is not clear what the values $n \cdot \tilde{V}_i^{n+1}$, $i = 1, 2, 3$, should be at the boundary. However, by assuming impermeability at the boundary for the divergence-free components, $\tilde{V}_2^{n+1}$ and $\tilde{V}_3^{n+1}$ only, we get

$$\begin{aligned}\left.\frac{\partial S}{\partial n}\right|_{\partial\Omega} = n \cdot \tilde{V}_1^{n+1}|_{\partial\Omega} &= n \cdot \tilde{V}^{n+1}|_{\partial\Omega} \\ &= n \cdot F(V)^n|_{\partial\Omega} \\ &= n \cdot \left.\frac{\partial p}{\partial n}\right|_{\partial\Omega}.\end{aligned}$$

Thus $S \equiv p\Delta t$, and so $W_1^{n+1} = V^{n+1}$. Also, from the above assumptions on impermeability at the boundary, we see that

$$\tilde{V}_3^{n+1} \equiv 0,$$

and so $W_2^{n+1} = W_1^{n+1} = V^{n+1}$.

This analysis demonstrates that in order to resolve the uniqueness question for an incompressible flow simulation it is sufficient to impose an impermeability constraint of the boundary on the divergence-free components only.

2.3.3. *Effect of Inexact Incompressibility*

Recall that the exact solution to the pressure equation

$$DG(p^{n+1}) = DF(V^n)$$

ensured a divergence-free flow at time step $n+1$. A relaxation of this incompressibility condition could be used as a means of reducing the costs of computation. For example, a scheme could be devised in which the pressure equation is not solved at every time step, but instead is solved at every mth time step, for some predetermined or variable m. Such schemes have been, in fact, used in certain flow simulations (see Gresho, Lee, and Sani [8]).

To observe the effects of violating the incompressibility condition, we computed (see also Gustafson and Halasi [9]) the following perturbed pressure equation

$$D \cdot G(p^*) = D \cdot F(V^n) + \varepsilon r,$$

where $\varepsilon r(x, y) = \alpha \cdot (x + y)$. Of interest was the range of α for which the perturbed flow still bore a resemblance to the corresponding divergence-free flow. Criteria

TABLE II

Effect of Pressure Equation Perturbation on Driven Cavity Flow at Time $t = 1$ Second, $Re = 10$

$\varepsilon r \equiv \alpha(x+y)$	$D(V)$	$V_{g.c}$	KE	p	$\|V^n - V^{n+1}\|_\infty$
$\alpha = 0.0$	$O(10^{-11})$	(0.206, 0.018)	130.7	$O(-4.0)$	$O(10^{-5})$
$\alpha = 0.04$	$O(10^{-4})$	(0.206, 0.018)	130.6	$O(-4.0)$	$O(10^{-5})$
$\alpha = 0.40$	$O(10^{-3})$	(0.206, 0.018)	130.7	$O(-4.0)$	$O(10^{-5})$
$\alpha = 2.00$	$O(10^{-2})$	(0.207, 0.017)	130.8	$O(-5.0)$	$O(10^{-6})$
$\alpha = 4.00$	$O(10^{-2})$	(0.208, 0.016)	131.1	$O(-6.0)$	$O(10^{-6})$

TABLE III

Effect of Pressure Equation Perturbation on Driven Cavity Flow at Time $t = 20$ Seconds, $Re = 400$

$\varepsilon r \equiv \alpha(x+y)$	$D(V)$	$V_{g.c.}$	KE	p	$\|V^n - V^{n+1}\|_\infty$
$\alpha = 0.0$	$O(10^{-11})$	0.104, 0.073)	144.3	$O(-4.0)$	$O(10^{-4})$
$\alpha = 0.04$	$O(10^{-2})$	(0.105, 0.072)	144.3	$O(-4.0)$	$O(10^{-4})$
$\alpha = 0.40$	$O(10^{-2})$	(0.114, 0.053)	144.6	$O(-4.0)$	$O(10^{-4})$
$\alpha = 0.80$	$O(10^{-1})$	(0.124, −0.041)	144.7	$O(-4.0)$	$O(10^{-4})$
$\alpha = 2.0$	$O(10^{-1})$	(0.160, −0.007)	142.6	$O(-5.0)$	$O(10^{-4})$

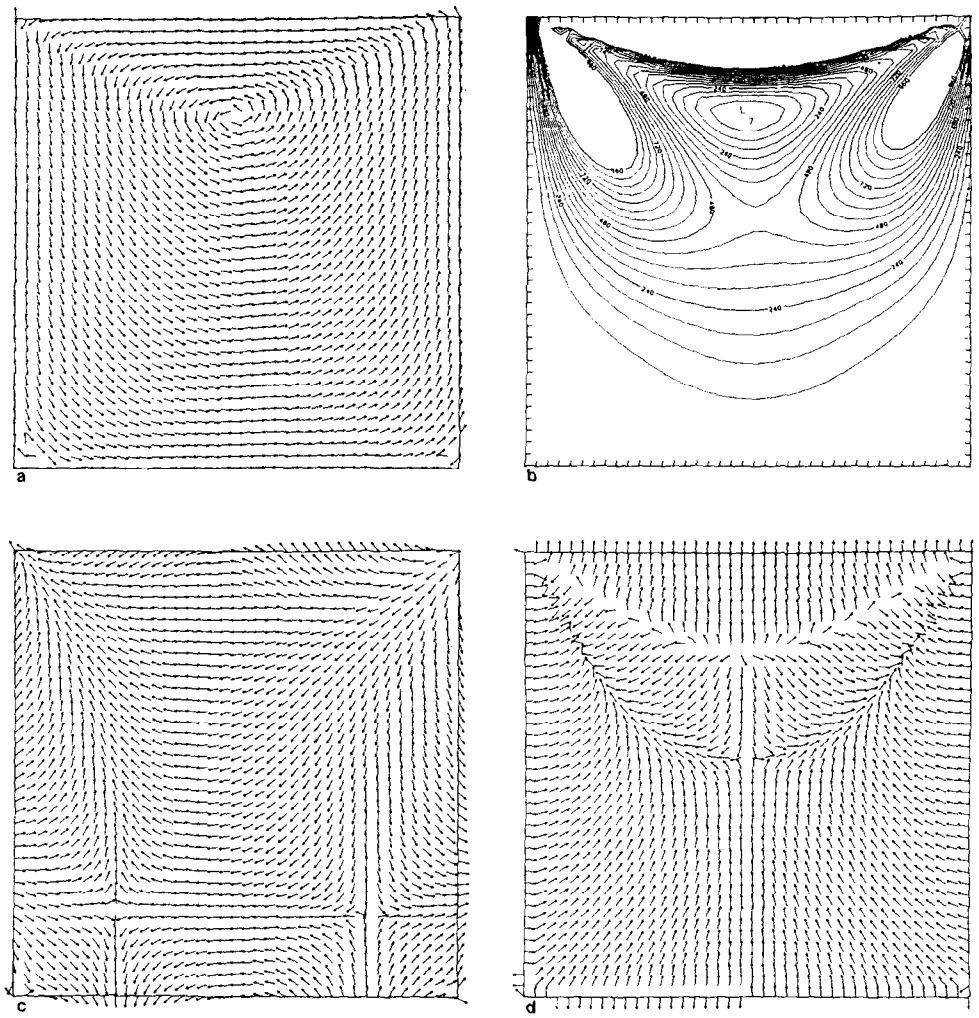

FIG. 5. Incompressibility maintained, Re = 10, $t = 1$ s. (a) Normalized velocity field. (b) Kinetic energy contours, labels scaled by 10,000. (c) Normalized pressure gradient. (d) Normalized kinetic energy gradient.

used in ascertaining flow resemblance included the geometry of the flow itself along with the geometries of the pressure gradient and kinetic energy distributions. Quantitative features, such as total kinetic energy and locations of eddy centers, were also measured and compared. Flows of Reynolds numbers 10 and 400 were perturbed in this manner. In all cases, the region of flow was the unit cavity upon which was superimposed a uniform mesh of cell length 1/40. In Tables II and III we exhibit some effects of these pressure equation perturbations.

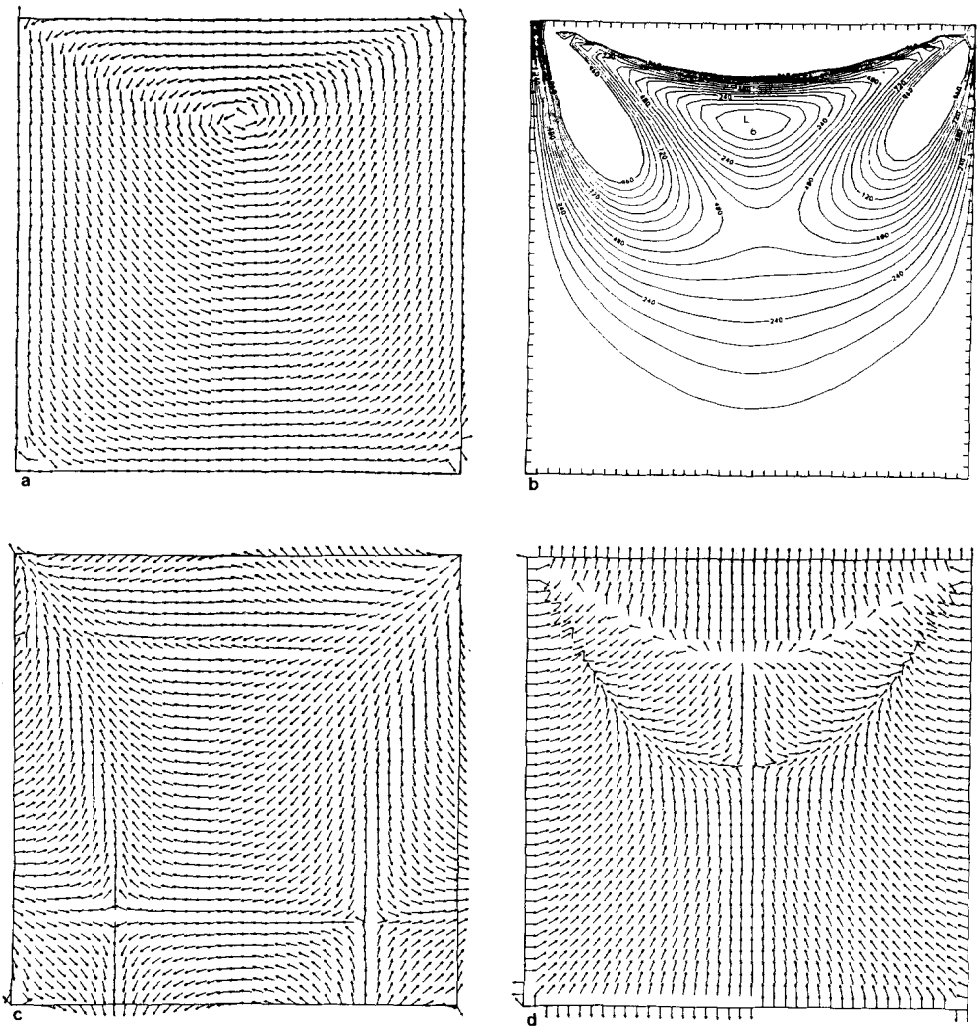

FIG. 6. Incompressibility disrupted, $Re = 10$, $t = 1$ s, $\alpha = 4.0$. (a) Normalized velocity field. (b) Kinetic energy contours, labels scaled by 10,000. (c) Normalized pressure gradient. (d) Normalized kinetic energy gradient.

In Tables II and III above, $V_{\text{g.c.}}$ indicates velocity at the geometric center of the cavity, KE is the kinetic energy of the entire flow, and p and $D(V)$ are roughly global values of pressure and divergence, respectively. Finally, $\| V^n - V^{n+1} \|_\infty$ is an indication of the convergence rate at the time step n corresponding to the time at which the effects are recorded. Graphic illustrations of some of these perturbation flows are found in Figs. 5–8.

In reporting these observed insensitivities re exact incompressibility, we would

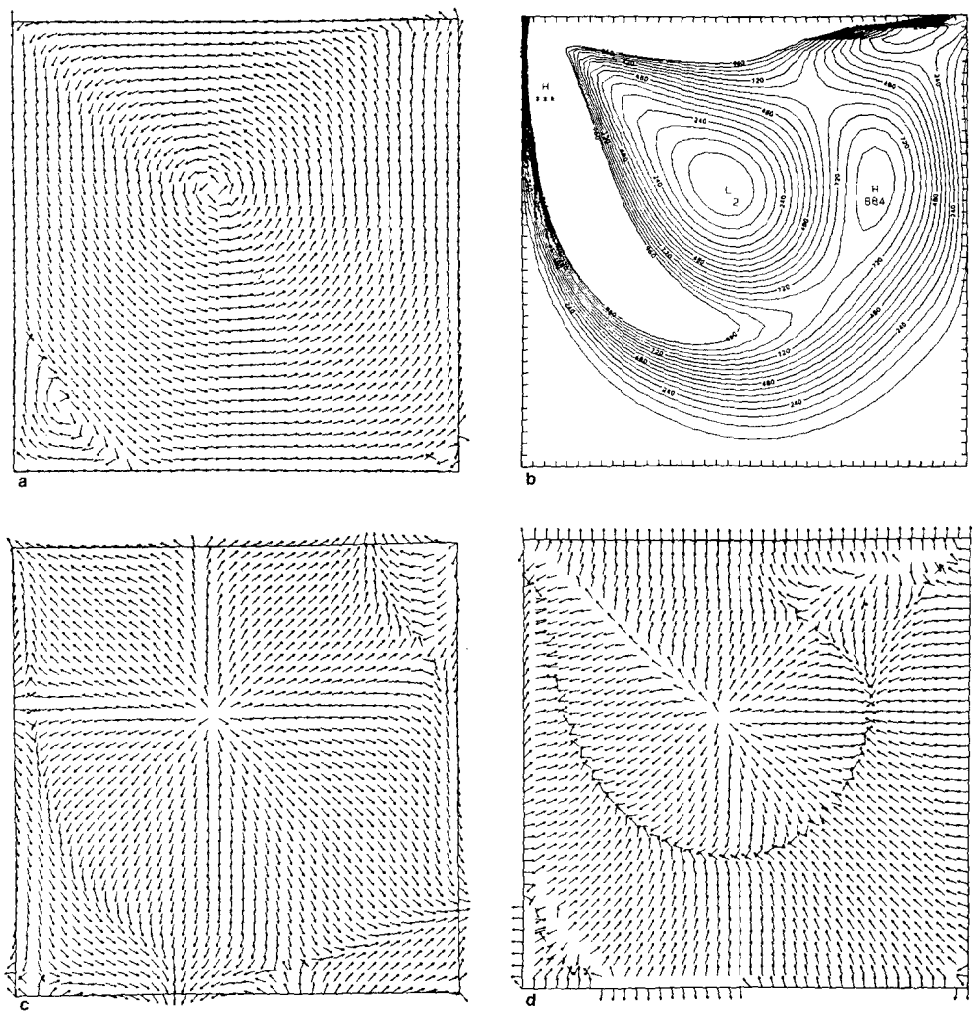

FIG. 7. Incompressibility maintained, $Re = 400$, $t = 20$ s. (a) Normalized velocity field. (b) Kinetic energy contours, labels scaled by 10,000. (c) Normalized pressure gradient. (d) Normalized kinetic energy gradient.

like to note on the other hand that (i) convergence may be slower, (ii) the primary vortex is further displaced, and (iii) increasing α caused some dissolution of the lower right corner eddy (see Fig. 6).

We also investigated the effect of perturbation of the pressure boundary data. For example, at $Re = 400$ we replaced the correct left boundary condition $p' = p + 2u/\delta x\, Re$ in the $(1, j)$ leftmost cells to

$$p'_{\text{pert}} = p' + 0.001(1 + j)$$

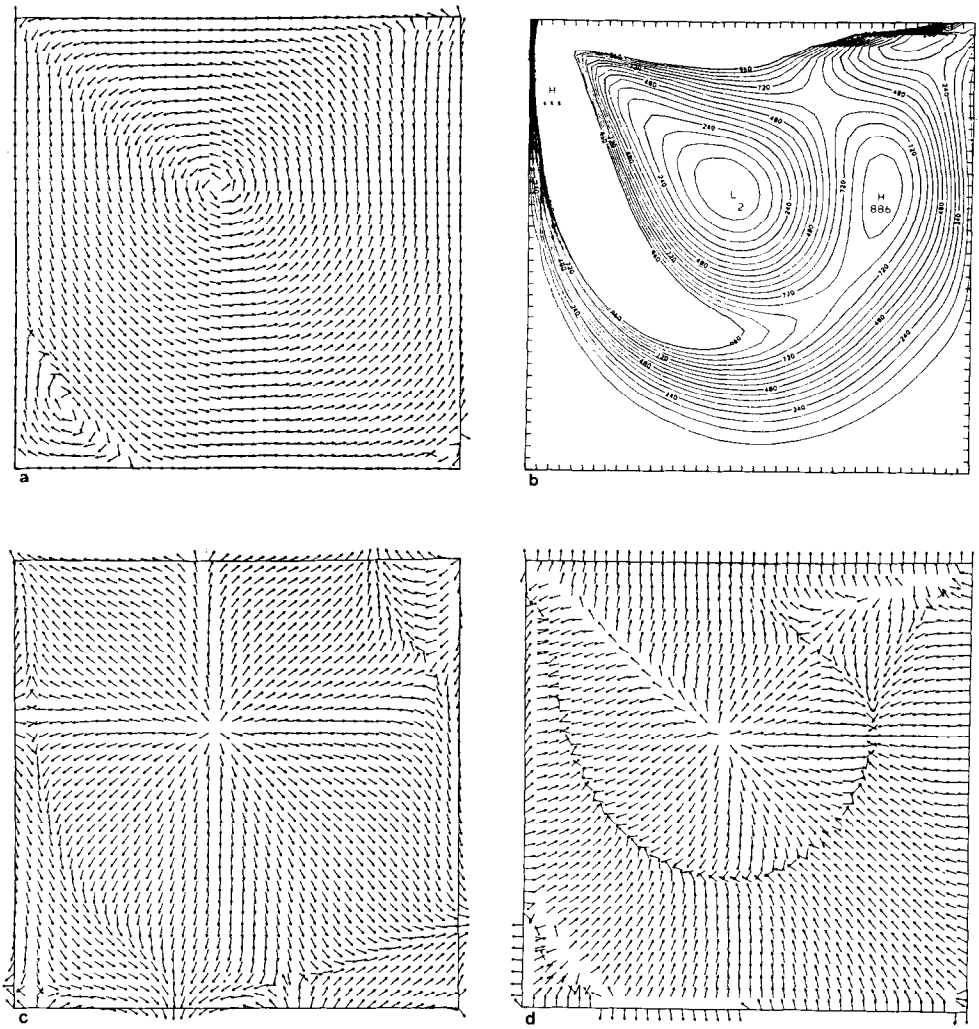

FIG. 8. Incompressibility disrupted, $Re = 400$, $t = 20$ s, $\alpha = 0.04$. (a) Normalized velocity field. (b) Kinetic energy contours, labels scaled by 10,000. (c) Normalized pressure gradient. (d) Normalized kinetic energy gradient.

and ran the flow to $t = 20$ seconds, which, although not yet steady, is well developed. The $(2, j)$ cells, i.e., the leftmost column of interior cells, did not conserve mass, to an error of $O(10^{-3})$. Elsewhere in the interior mass was preserved to $O(10^{-11})$. The center velocity $V_{g.c.}$ was (0.104, 0.074), very close to the unperturbed case (see Table III). Similarly, global kinetic energy (144.2), global pressure $O(-3)$, and convergence rate ($O(10^{-4})$) were close to those of the unperturbed flow.

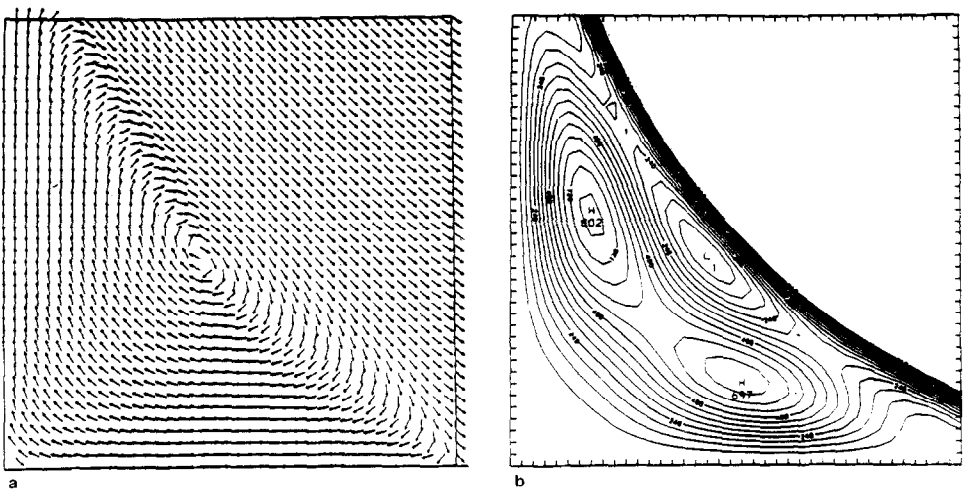

FIG. 9. Lower left corner detail. (a) Normalized velocity field. (b) Kinetic energy contours, labels scaled by $0.1E+08$.

2.4. *Enhancement by Kinetic Energy Portraits*

The use of kinetic energy contours and normalized kinetic energy gradient flows was investigated as an alternative way of isolating qualitative behavior patterns present in cavity flows. See, for example, Fig. 9, where, even though we detected a lower left corner tertiary eddy at relatively low Reynolds numbers (e.g., $Re=400$) and resolution (e.g., 150×150) from the velocity flow alone, much more detail is brought out by kinetic energy enhancement.

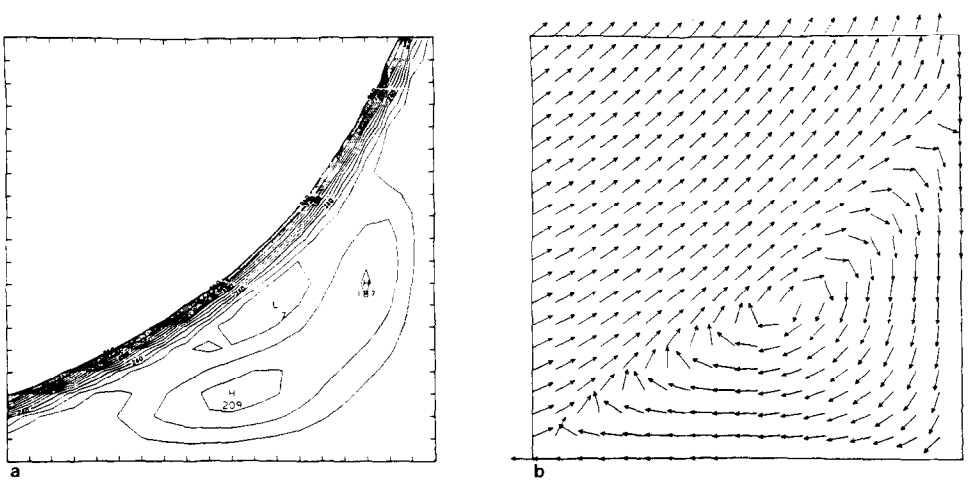

FIG. 10. Lower right corner detail. (a) Kinetic energy contours, labels scaled by $0.1E+10$. (b) Normalized velocity field.

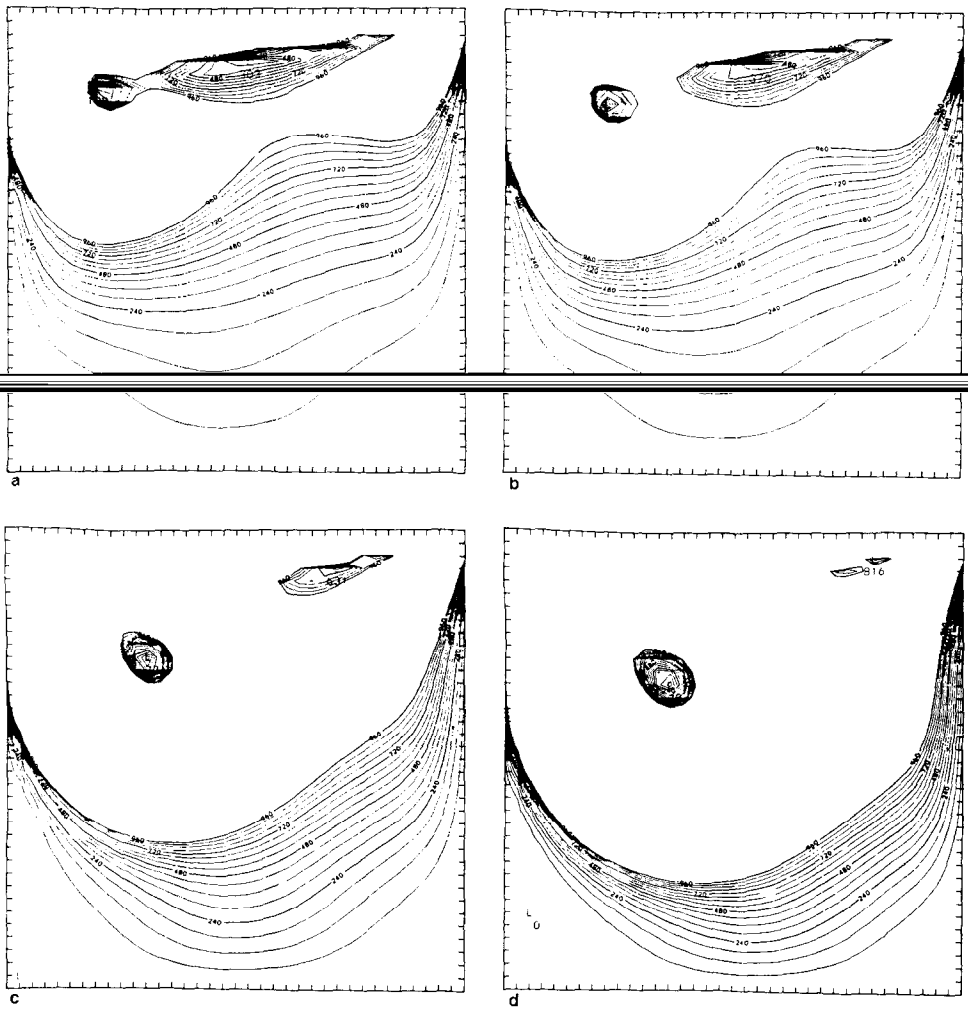

FIG. 11. Transient kinetic energy feature observed during central vortex development. $Re = 400$ and time runs from $t = 1.77$ s to $t = 4.02$ s. Labels scaled by $0.1E + 06$.

In the staggered mesh system used, the individual x and y components of the velocity field are segregated from each other. Thus, in order to graphically plot the velocity field it was therefore necessary to reassign the velocity components to a common point. This was achieved by averaging the y-component horizontally and the x-component vertically. In this manner, velocity vectors are defined at the corners of the computational cells. From these values one obtains the kinetic energy contours and gradients.

A finer vortex structure was revealed by the presence of two sites of relative high energy adjacent to the centers of the vortices. These neighboring local maximum

sites are more noticeable with the corner eddies, Figs. 9 and 10, than with the primary vortex, Fig. 2. Of particular note, from the kinetic energy gradient flow, e.g., Figs 5 and 7, one observes a ridge of local maximum energy partially surrounding the primary vortex. Kinetic energy portraits also reveal features such as the transient "quasi-vortex" shown in Fig. 11. As time runs on the forming central vortex splits, the left portion becoming the principal. The transient portion soon disappears completely.

2.5. *Enhancement by Pressure Characteristics*

In general, a pressure equation for the flow within any geometric configuration is obtained by applying the divergence operator to the Navier–Stokes equations. Since the flow is assumed incompressible we have

$$-\nabla^2 p = \nabla \cdot (V \cdot \nabla V).$$

In the absence of this nonlinear term (i.e., Stokes flows) there results, likewise, an absence of a density distribution for the conservative force field ∇p. On the other hand, in non-Stokes flow regimes, the effect on the pressure gradient ∇p is that it now is the result of superposing sinks and sources of density $-\nabla^2 p = \nabla \cdot [(V \cdot \nabla) V]$. In Figs. 5 and 7 we observe the effects of this nonlinearity (or the lack of it) in the behavior of the pressure gradient field.

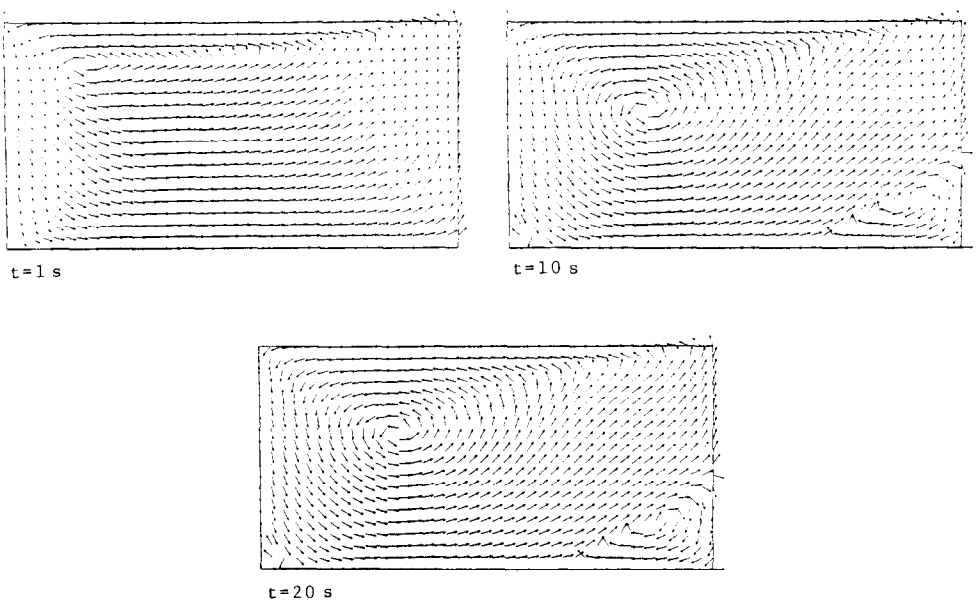

FIG. 12. Flow in cavity of aspect ratio $A = 0.5$, $Re = 400$. At $t = 20$ s $\|V^n - V^{n-1}\|_\infty = O(10^{-13})$.

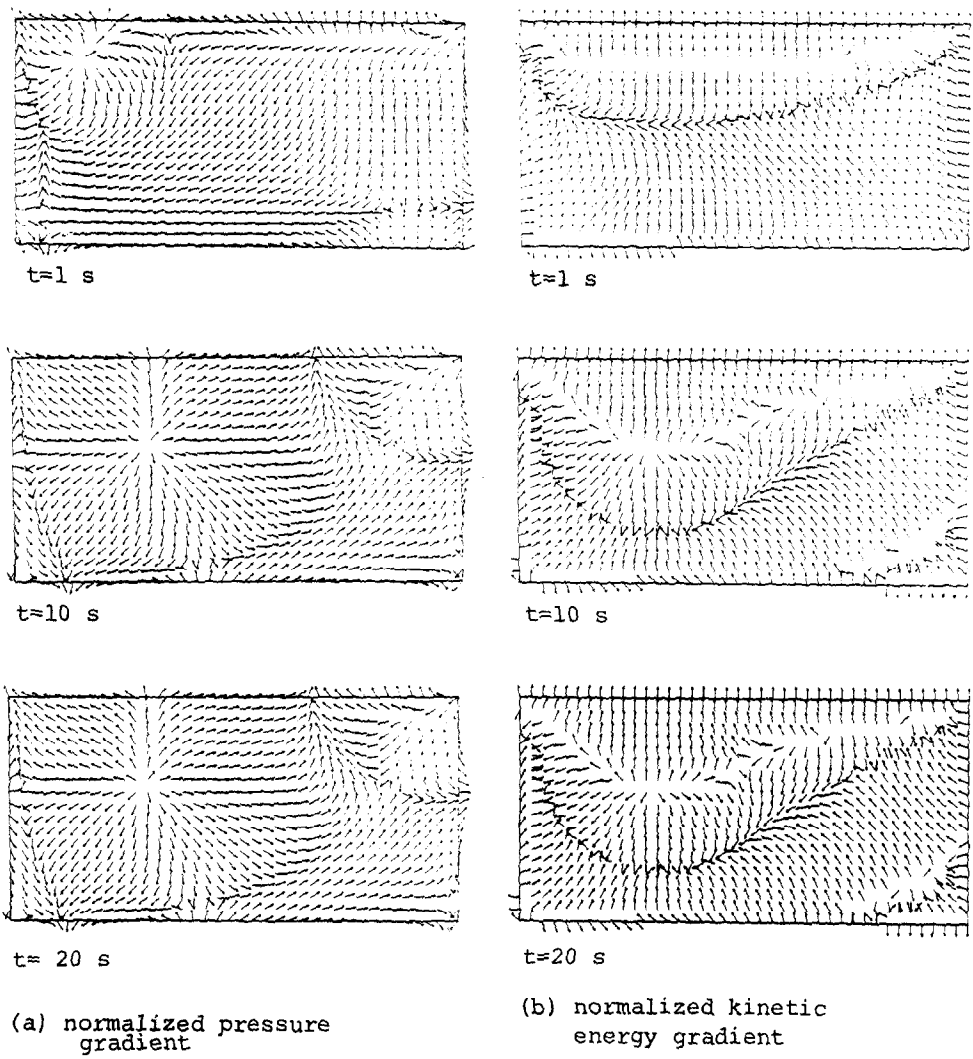

FIG. 13. Additional flow characteristics at $A = 0.5$, $Re = 400$.

That similar sources are not associated with the secondary corner eddies can be explained by arguing that within such regions the characteristic velocities are relatively low. In such regions the effective Reynolds number will be lower. Similarly in deep cavities the pressure diagrams for the secondary principal vortices revealed no significant sources. See the figures in Section 3. Computationally this denigration of source might appear to be improperly enhanced by the multiplication by small values of Δt in (2.12) but this should be counterbalanced by the multiplication by $(\Delta t)^{-1}$ in (2.13).

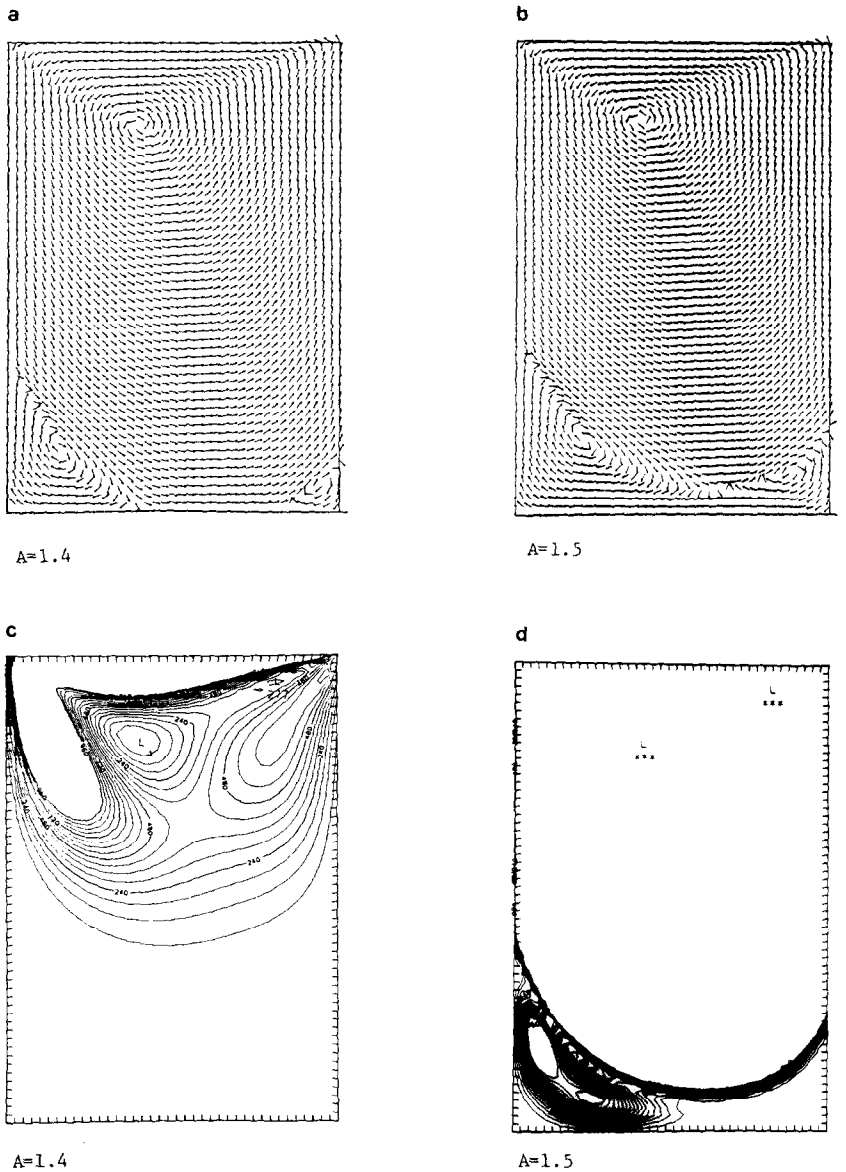

FIG. 14. Incomplete and nearly complete eddy fusion for $Re = 100$ at aspect ratios $A = 1.4$ (left) and $A = 1.5$ (right), respectively. Time $t = 15$ s. $A = 1.4$, kinetic energy contours, labels scaled by 10,000. $A = 1.5$, kinetic energy contours, labels scaled by $0.1E + 10$.

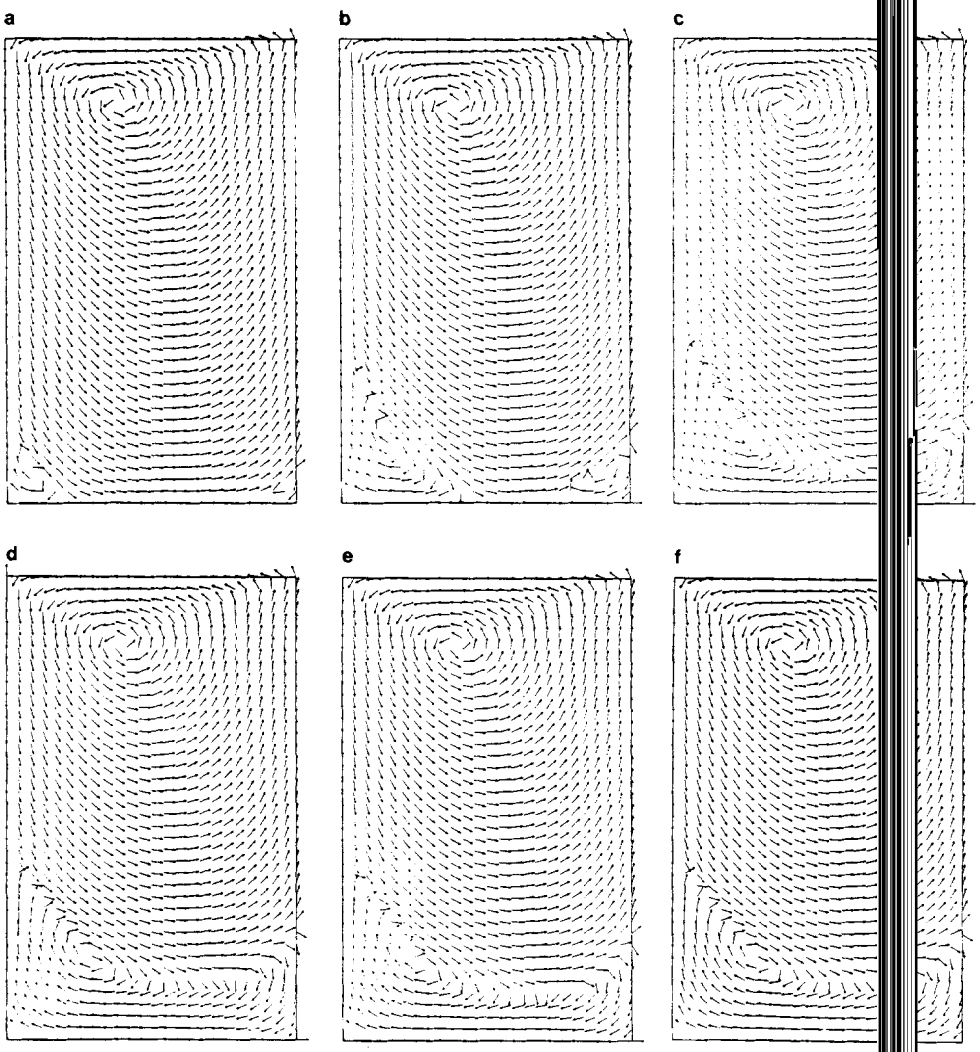

FIG. 15. Complete corner eddy fusion for $Re = 100$ at aspect ratio $A = 1.6$: (a) 4 s; (b) 6 s; (c) 8 s; (d) 10 s; (e) 20 s; (f) 30 s.

3. VORTEX DYNAMICS OF UNSTEADY FLOW

Features of steady flow in the unit two-dimensional cavity have been extensively studied and documented over the years (see Table I). The thrust of earlier investigations was to exhibit and study the ambulatory nature of the primary vortex center as the Reynolds number varied. The later demonstration of secondary corner eddies and their relative sizes, both with respet to one another as well as the primary vortex, depended upon the advent of higher-quality computational

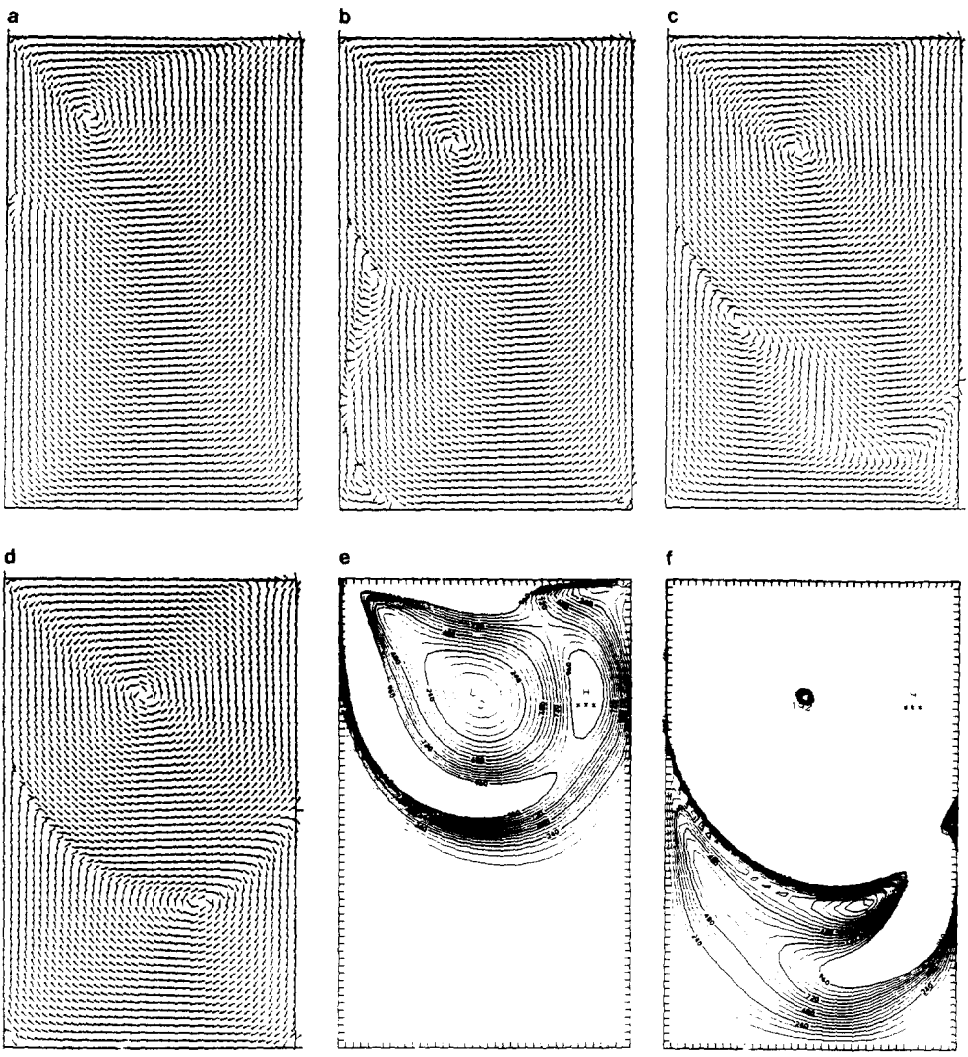

FIG. 16. Velocity and kinetice energy features of complete eddy fusion for $Re = 800$ at aspect ratio $A = 1.6$: (a) 4 s; (b) 8 s; (c) 12 s; (d) 40 s; (e) 40 s, labels scaled by 10,000; (f) 40 s, labels scaled by $0.1E+07$.

methods and machines, which permitted the observation of tertiary corner eddies as well. However, the actual genesis of these increased details of steady flow remained wanting.

Recent unsteady flow simulations, such as Gatski *et al.* [6] and the present paper, permit not only a better understanding of the steady flow, i.e., the fluid statics as a limit as $t \to \infty$ of the flow evolution, but also, more importantly perhaps, provide details of the fluid dynamics itself. Among our findings:

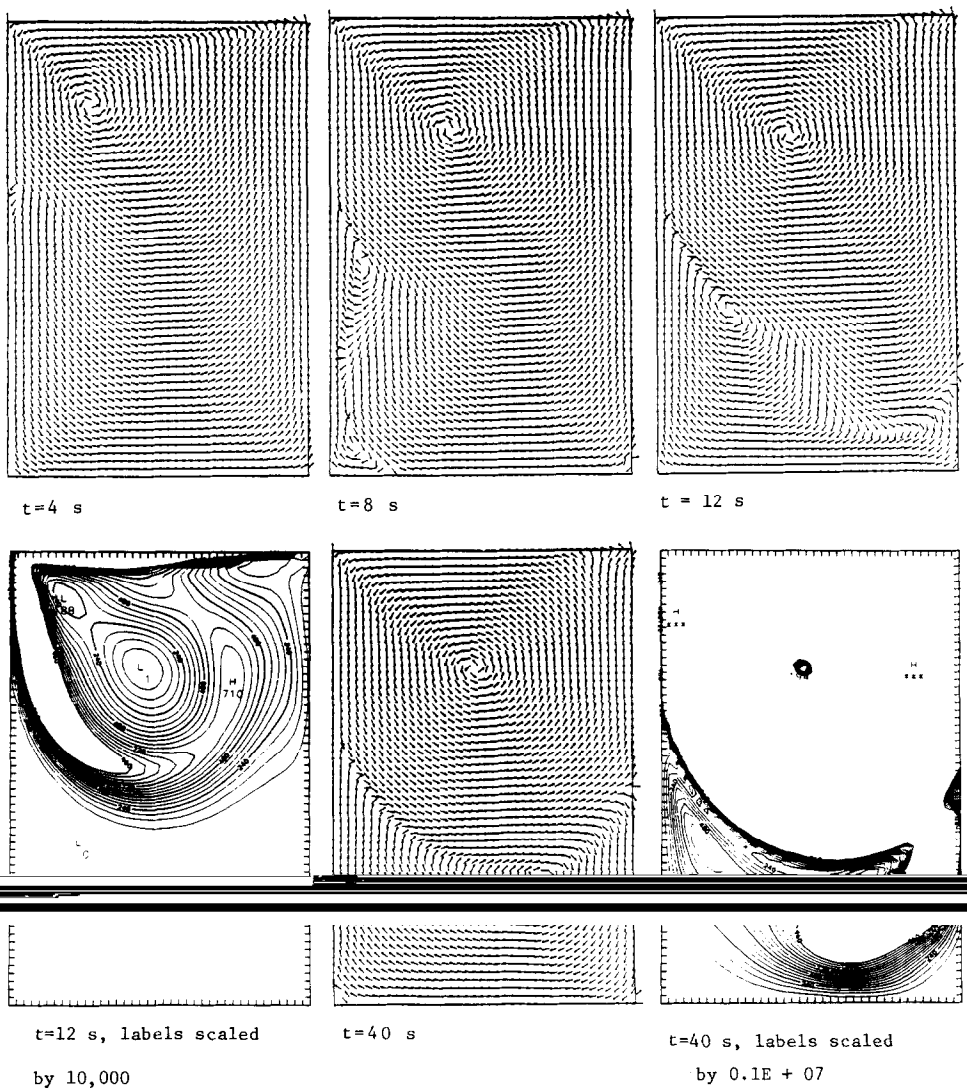

FIG. 17. Velocity and kinetic energy features leading to eddy fusion for $Re = 800$ at aspect ratio $A = 1.5$.

(a) The topology of the vortex formation, first the primary vortex and then only shortly afterward the secondary characteristics, develops almost immediately. The amplitudes develop much more slowly. One sees this much more rapid qualitative development even on relatively coarse meshes.

(b) For aspect ratio 2, at moderate Reynolds numbers a wall eddy forms just before the downstream corner eddy does. Later there is a coalescence, originally between these two eddies, and then with the upstream corner eddy. We cannot be

certain, due to resolution limitations, that the wall eddy is independent of some as yet unseen boundary layer connection from the separation point down to the corner eddy.

(c) Nonlinear Stokes flow (e.g., $Re = 10^{-6}$) final states are attained by linear Stokes flow at higher Reynolds numbers (e.g., $Re = 400$) but the latter take much longer to develop to the same states. These flows are characterized by a much more symmetric normalized velocity although the pressure profiles are somewhat less symmetric. This tendency toward symmetry precludes the wall eddy formation.

(d) All observed dynamic properties, e.g., principal vortex location and diameter evolution (a main object of the earlier steady investigations), secondary eddy sizes (a main object of more recent steady investigations), whether or not wall eddies form, and whether or not lower eddy coalescence is complete, are related in a functional dependence between the Reynolds number Re and the aspect ratio A.

One misses many intricacies of the eddy dynamics until one goes to deeper cavities, e.g., $A > 1.5$ (at $Re = 100$, for example). First, however, for comparison to Gatski *et al.* [6], we consider in Section 3.1 the case of shallow cavities, i.e., $A < 1$. In Section 3.2 we view the transition to eddy coalescence for intermediate cavities, e.g., $A = 1.4$, 1.5, and 1.6. Then in Sections 3.3 and 3.4 we turn to deeper cavities and to more detailed studies of specific observed dynamic eddy structures.

There is some lack of convention in the literature as to notation for the secondary eddies. We shall refer to the lower left corner eddy as the downstream, or first corner, eddy. The second, or right-hand corner, eddy will be referred to as the upstream eddy.

3.1. *Shallow Cavity Flows*

The dynamics to steady state of shallow cavity flow, $A = 0.5$, at $Re = 400$, were obtained in Gatski *et al.* [6]. In Figs. 12 and 13 we give our results for comparison to those of Gatski *et al.* Note that both here and in [6] the roles of the secondary corner eddies is reversed for $A = 0.5$, the dominant size and strength being shifted to the upstream eddy. This tendency is evident in the moderate Reynolds number range, but becomes increasingly less so as Re decreases to zero. Also of note is the large relative size of the primary vortex. This feature is shown, in particular, by the kinetic energy gradient field of the flow.

32. *Intermediate Cavity Flow*

Allowing the aspect ratio of the cavity to take on values larger than one presents further opportunities for secondary vortex behavior examination. This can be achieved, in general, without affecting the features of the primary vortex, as observed by Kawaguti [13]. This same author noted, in particular, the existence of a secondary flow region near the bottom of the cavity of aspect ratio $A = 2$. Such secondary flows were absent in instances where A was less than unity.

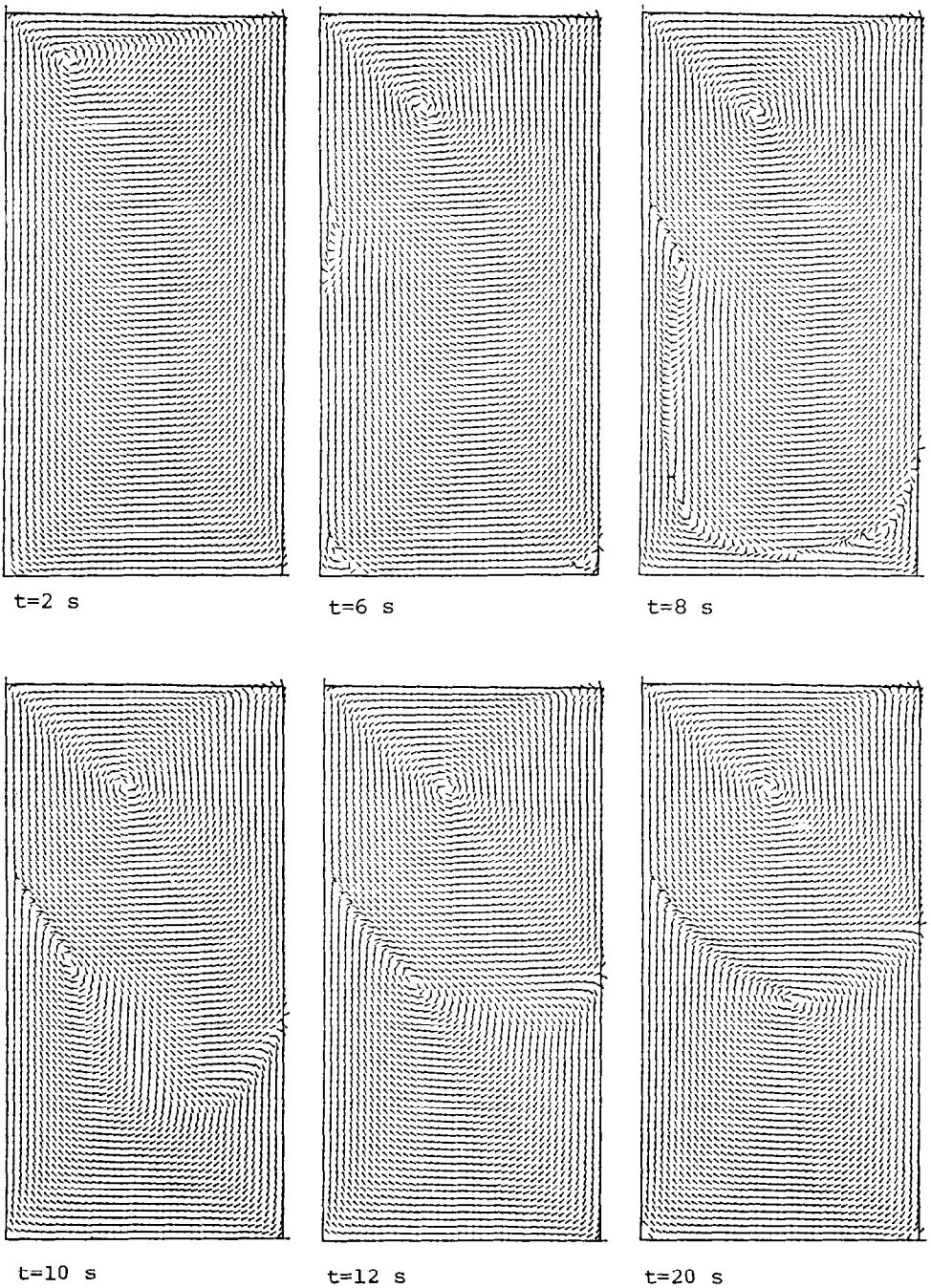

FIG. 18. Evolution toward near steady flow for $Re = 400$ at aspect ratio $A = 2.0$.

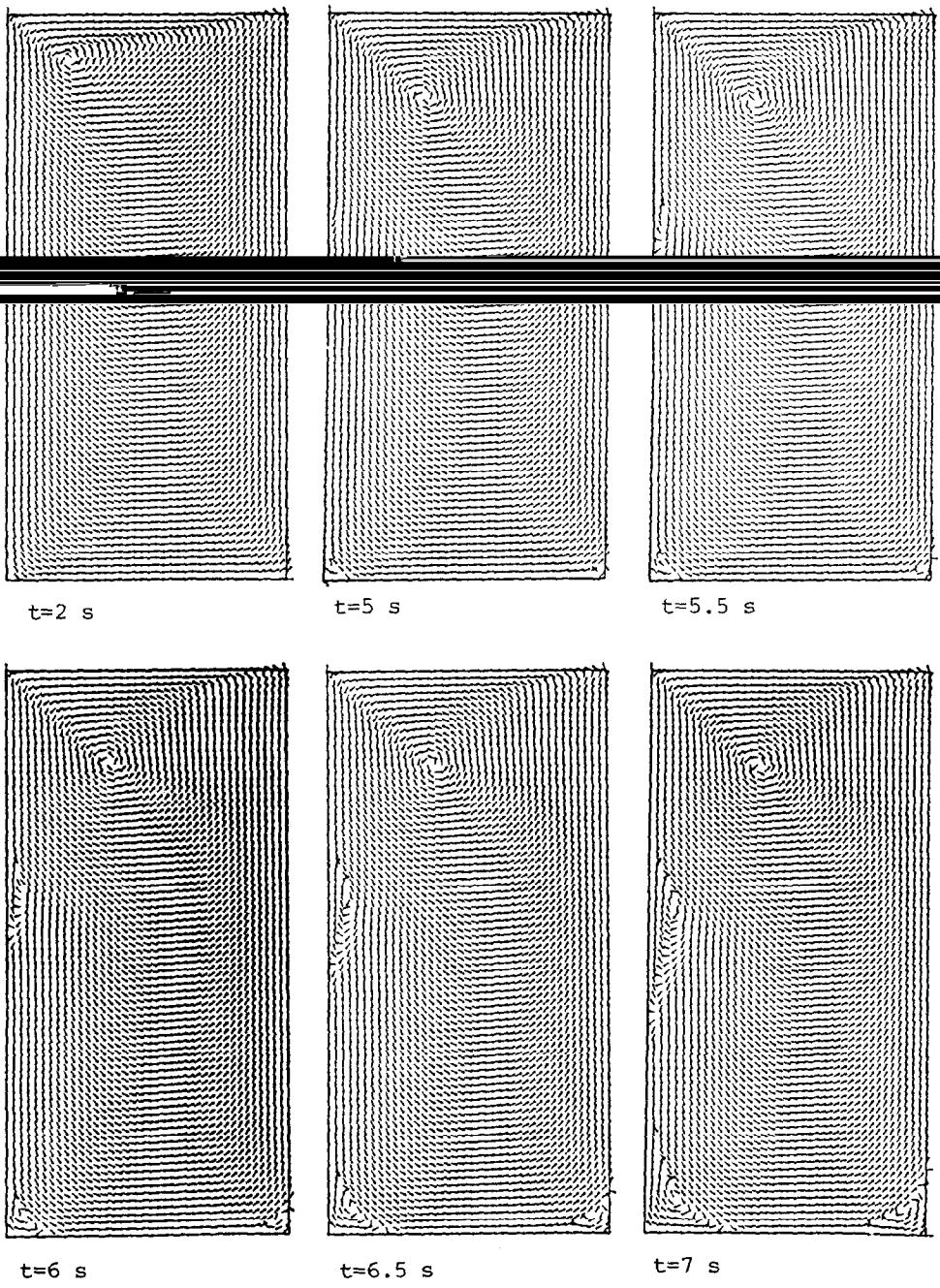

FIG. 19. Vortex dynamics involving wall eddy and corner eddies with kinetic energy contours for $Re = 400$ at aspect ratio $A = 2.0$.

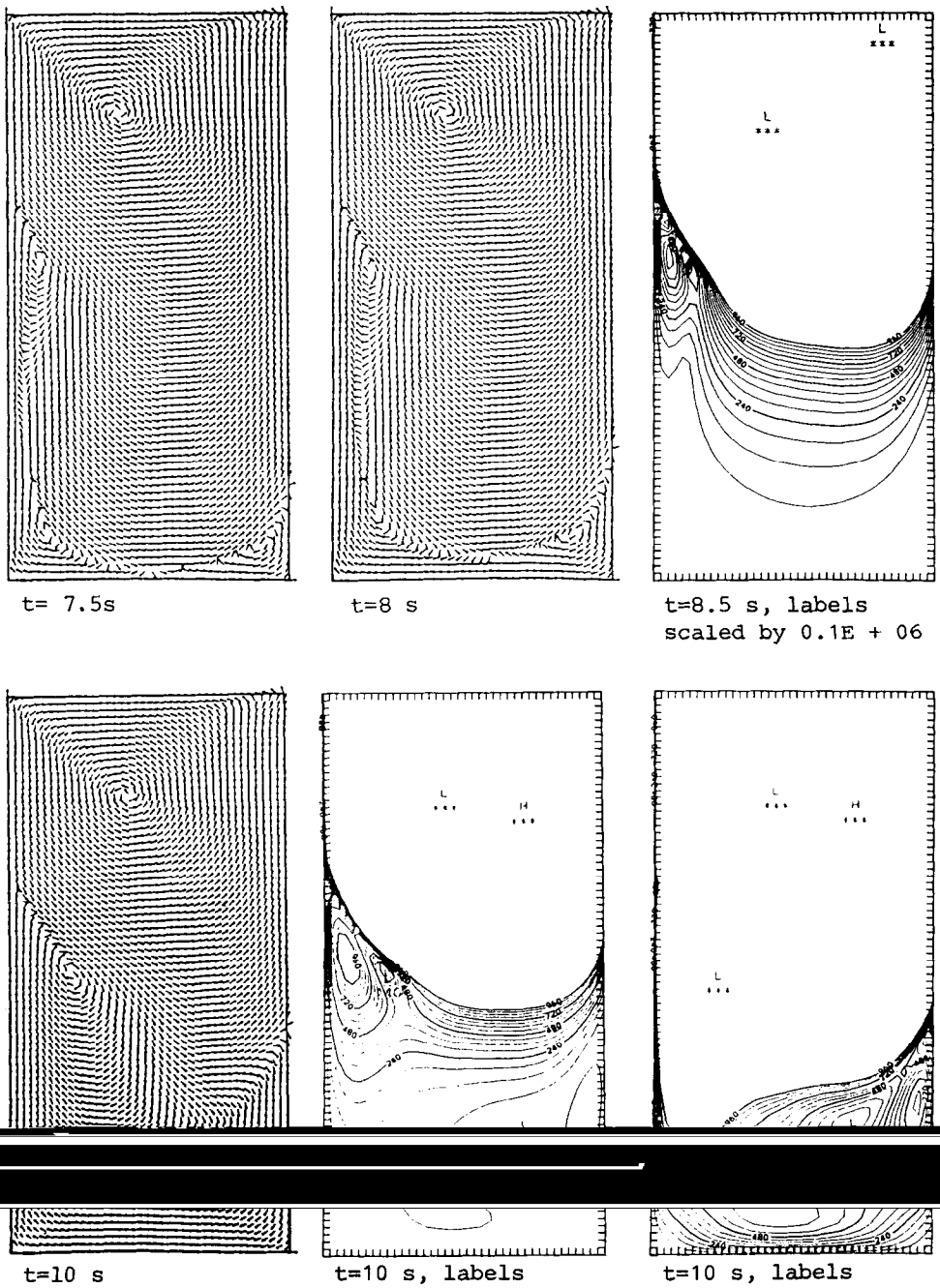

FIG. 19—*Continued.*

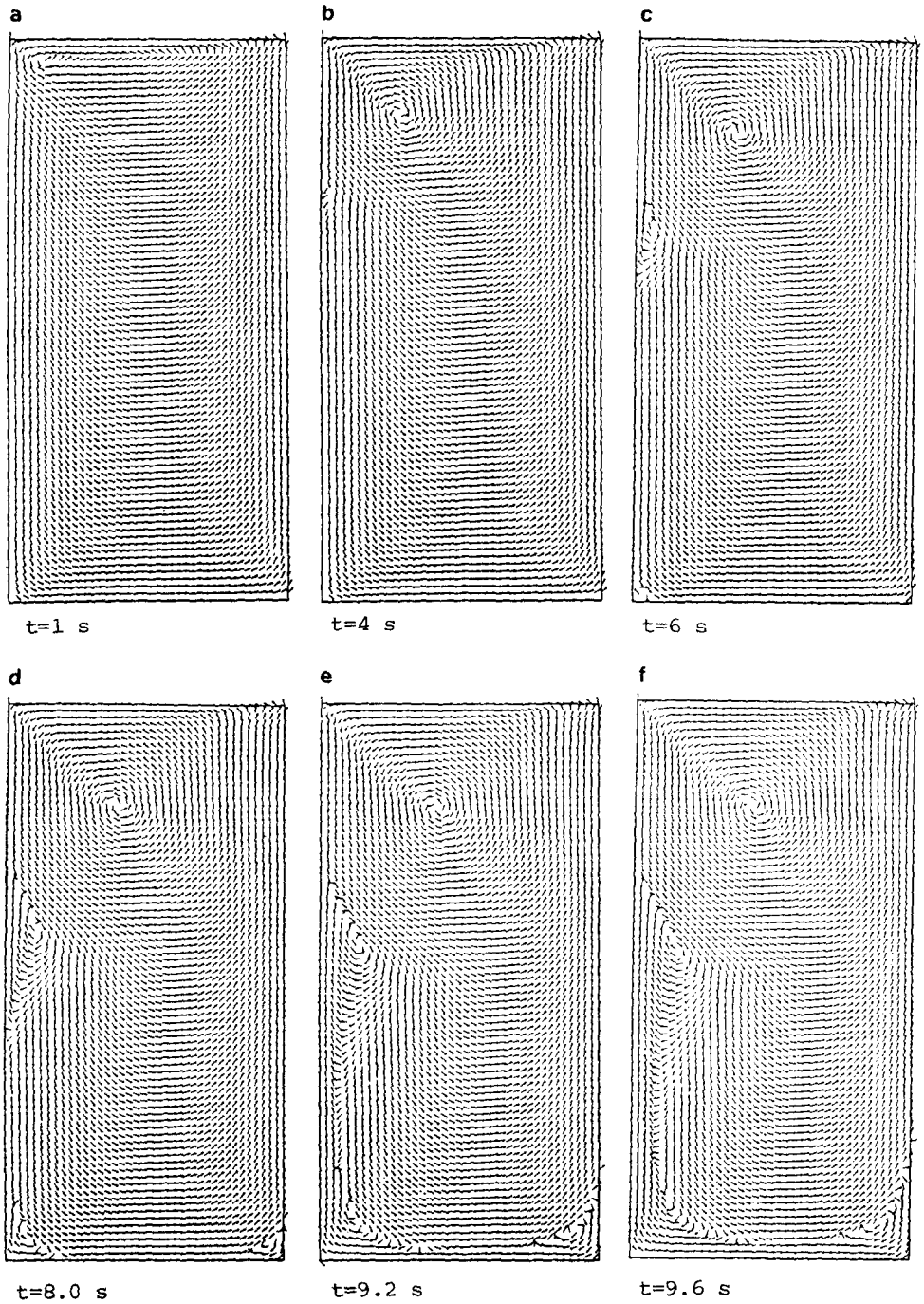

FIG. 20. Development of wall eddy for $Re = 800$ at aspect ratio $A = 2.0$.

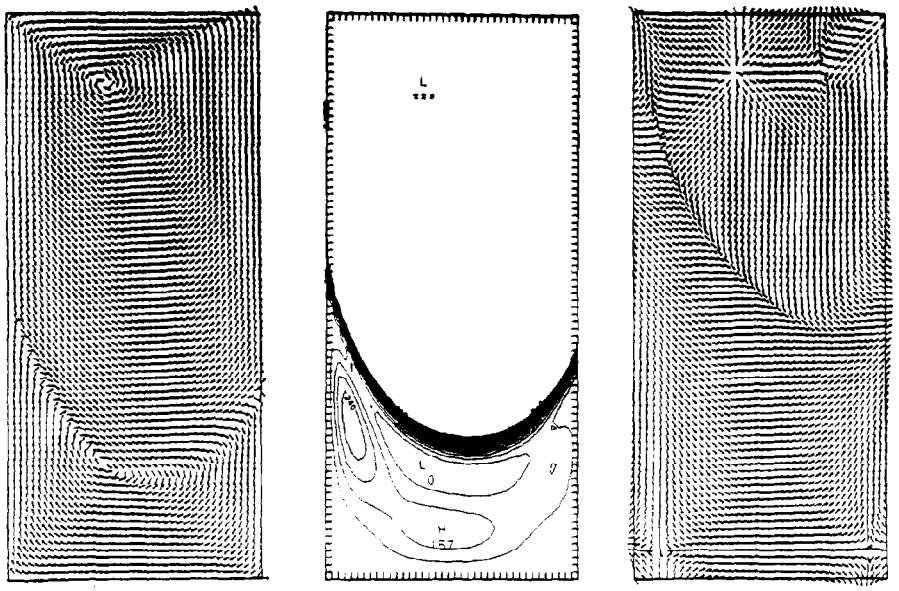

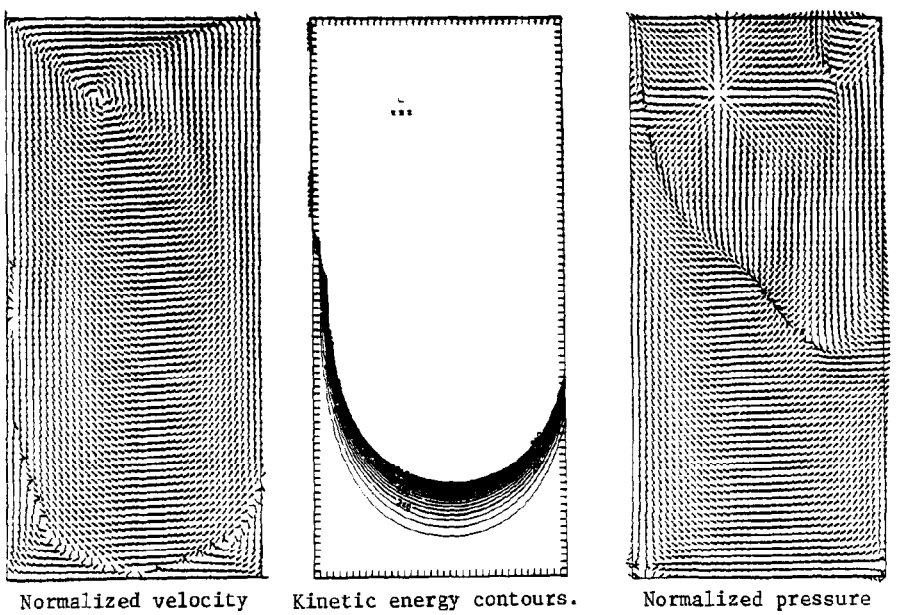

FIG. 21. Absence and presence of wall eddy for different Reynolds numbers at aspect ratio $A = 2.0$. (a) $Re = 100$, time $t = 6$ s. (b) $Re = 200$, time $t = 6$ s.

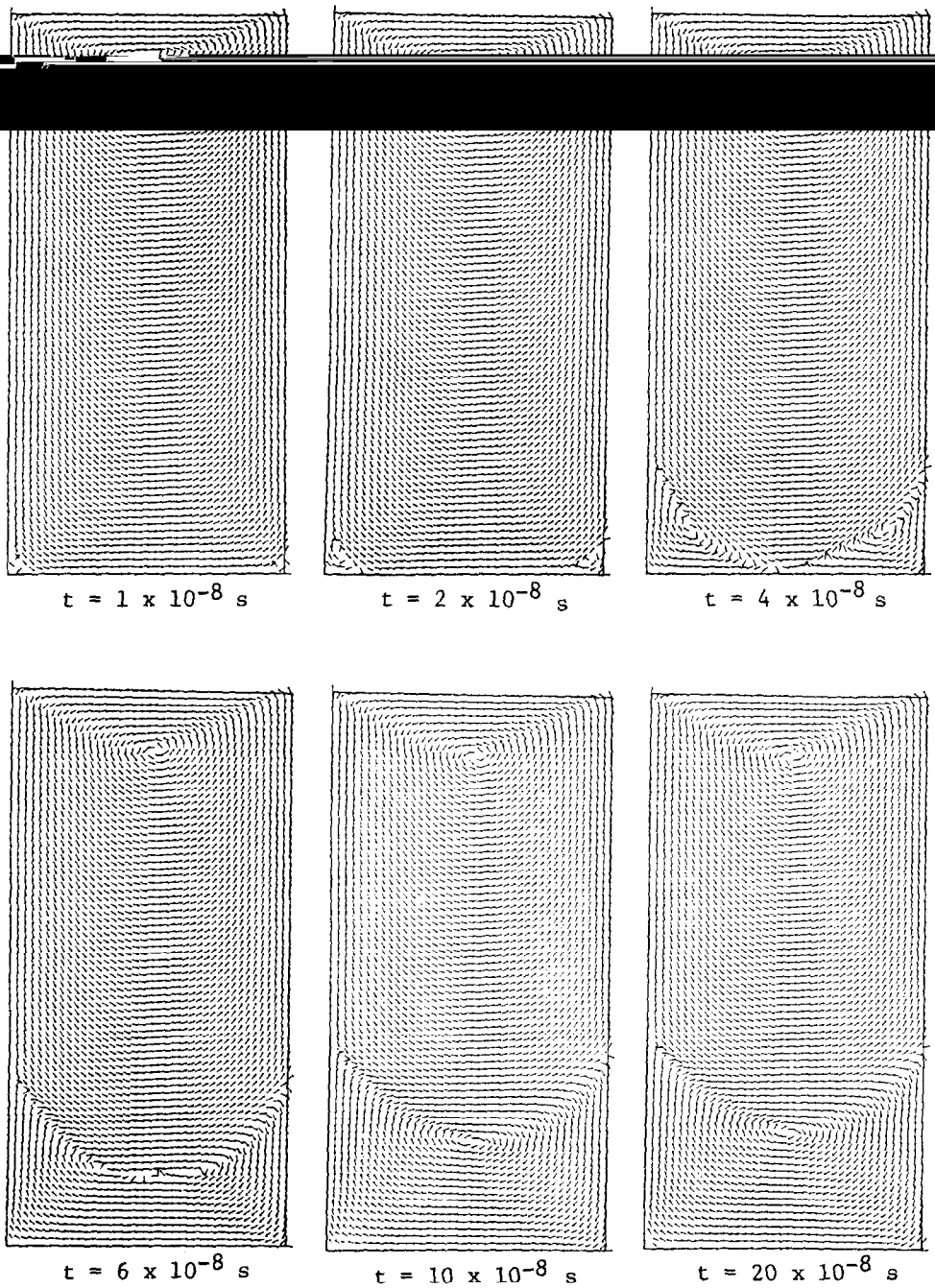

FIG. 22. Evolution of full nonlinear flow with $Re = 10^{-6}$ at aspect ratio $A = 2.0$.

Bozeman and Dalton [4] described these secondary regions of recirculation in terms of downstream corner eddy growth with increasing aspect ratio. At aspect ratio $A = 2$ they confirmed the Kawaguti finding of a secondary flow, which, however, is attributed to the growing downstream vortex occupying the entire lower region of the cavity. The Bozeman and Dalton studies include additional values of the aspect ratio in the intermediate range between one and two. Of particular note was that a secondary recirculation flow had already formed with aspect ratio $A = 1.6$. At aspect ratio $A = 1.4$ no such flow was found. These investigations were carried out at $Re = 100$.

For comparison of the unsteady limit of our dynamic analysis with the steady configuration found in Bozeman and Dalton, we ran the cases $A = 1.4$ and $A = 1.5$ at $Re = 100$. See Fig. 14. Note the quite clear failure of coalescence in the case $A = 1.4$. On the other hand the case $A = 1.5$ can be regarded as nearly complete coalescence into a secondary region of flow. For $A = 1.6$ we obtain (Fig. 15) an unsteady limit in close agreement to the stationary computation of Bozeman and Dalton [4, Fig. 7d].

Observing the evolution of the time-dependent flow regime permits a greater understanding concerning the formation of the secondary region of recirculation and its Reynolds number dependence. Figures 15 and 16 compare flow at $A = 1.6$ for $Re = 100$ and 800. For the latter, coalescence occurred more quickly and more completely. Figure 17 compares the flow at $A = 1.5$ for $Re = 800$ with the previous (Fig. 14) flow at $Re = 100$. Note the full coalescence at the higher Reynolds number.

3.3. *Secondary Eddy Separation and Coalescence*

As the aspect ratio of the cavity is further increased, additional dynamical information on basic eddy formation, growth, separation, and reintegration into the flow can be gained. We found that many of the fundamental mechanics may be seen at $A = 2$. Some observations on deeper cavities will be found in Sections 3.4 and 3.5, which will conclude the paper.

An unforeseen dynamical characteristic was the formation of a wall eddy (see Fig. 18). This also appeared in the dynamics of intermediate depth cavities (see Fig. 16 and 17). This eddy then coalesces with the two corner eddies to form a secondary circulation. More dynamical detail is given in Fig. 19. Note how this third secondary eddy forms on the downstream wall of the cavity and grows downward at a rate faster than two corner eddies, eventually interfering, and then fusing, with them.

Figure 20 demonstrates the wall effect as a function of Reynolds number, there $Re = 800$. Note how this wall eddy appears to develop prior to the downstream eddy. We observed this eddy for $Re = 200$ but it was not evident at $Re = 100$.

A closer comparison, including kinetic energy profiles and pressure gradients, of the flows at $Re = 100$ and $Re = 200$ is given in Fig. 21. Note the relative insensitivity, mentioned earlier, of the pressure gradient for distinguishing two quite different qualitative flows.

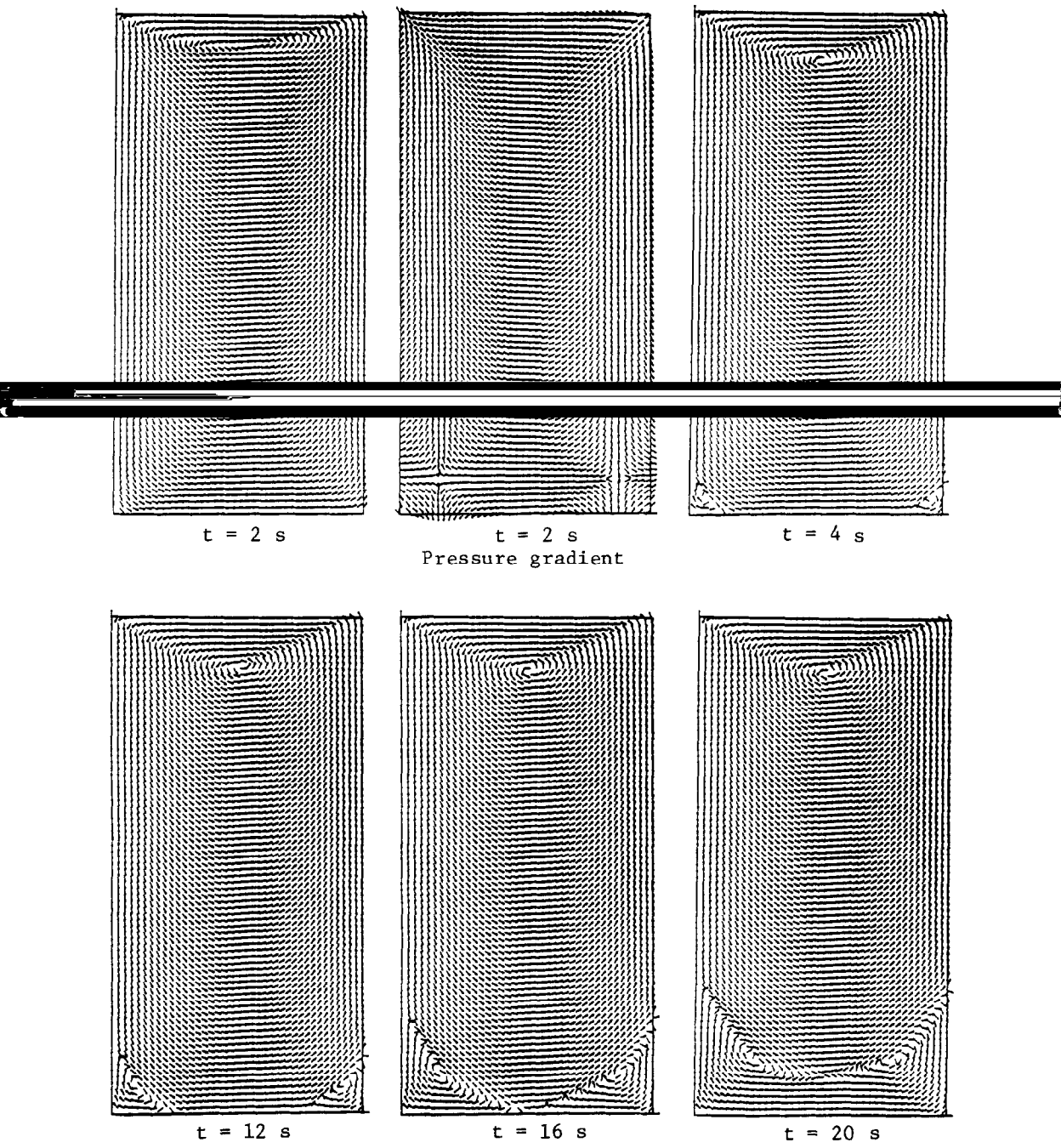

FIG. 23. Normalized velocity, normalized pressure gradient, and kinetic energy contours for linearized flow of $Re = 400$ at aspect ratio $A = 2.0$.

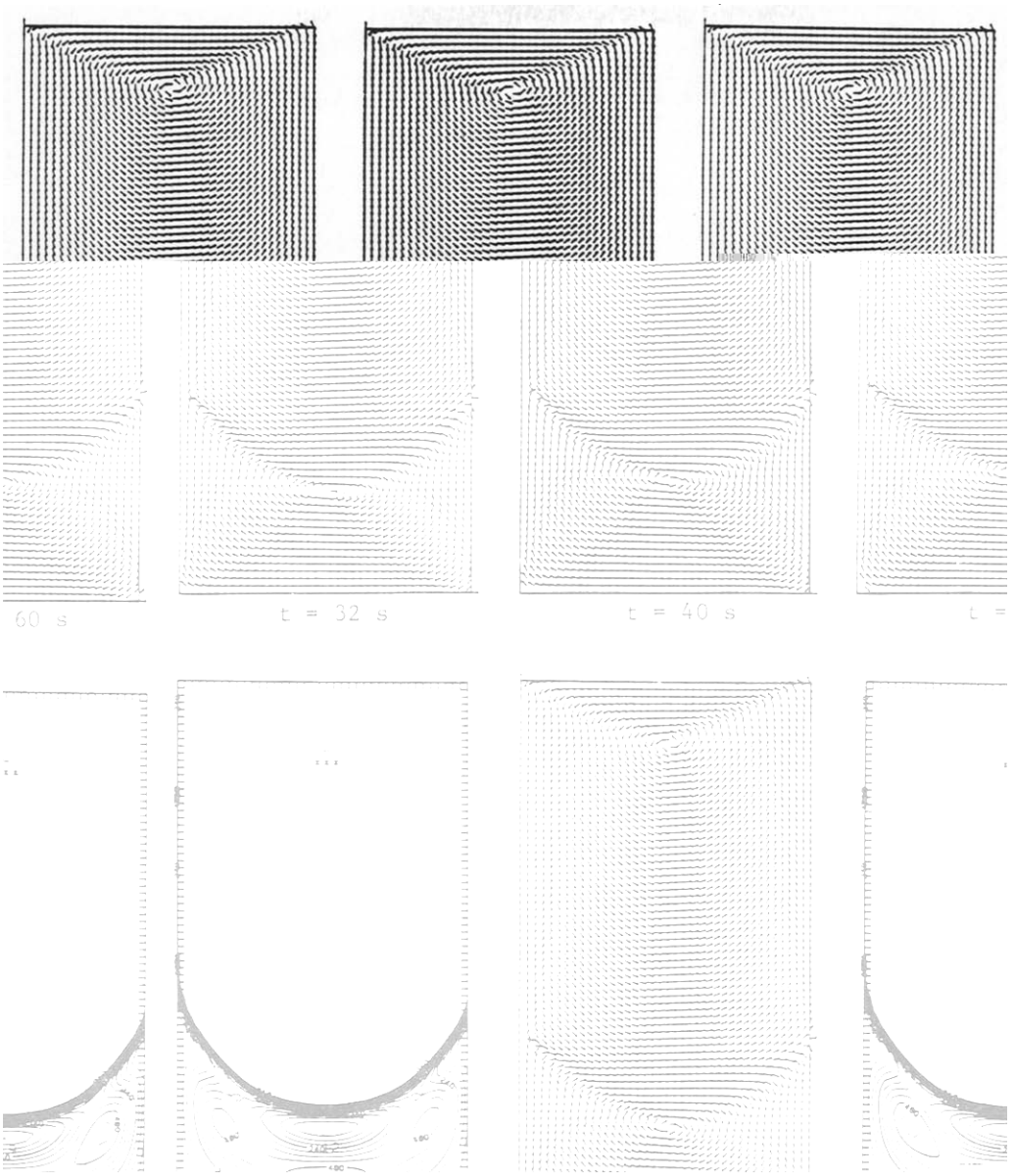

FIG. 23—*Continued.*

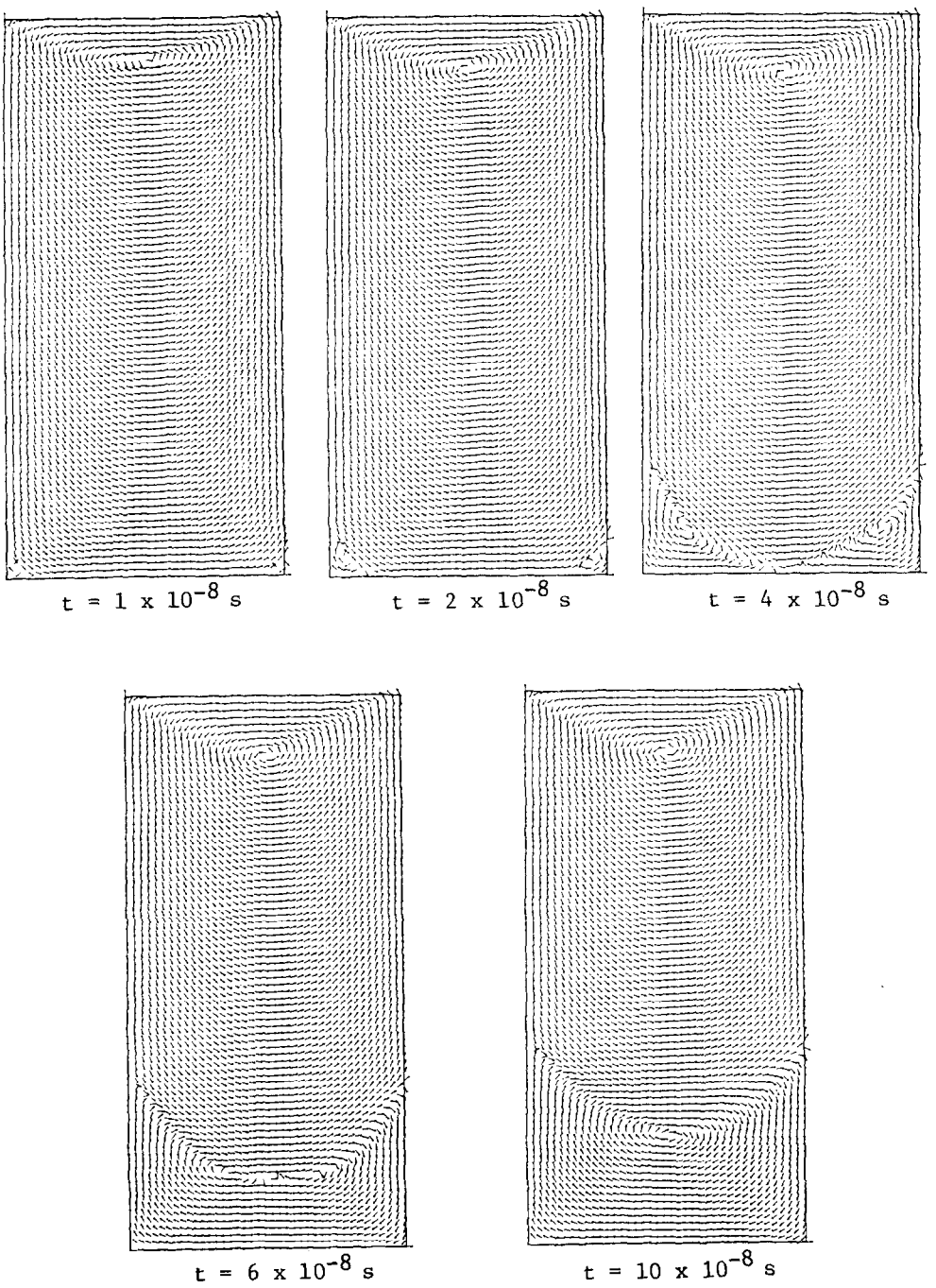

FIG. 24. Normalized velocity flow of linearized flow with $Re = 10^{-6}$ at aspect ratio $A = 2.0$.

The result of decreasing the Reynolds number to $Re = 10^{-6}$ is shown in Fig. 22. Although in all three cases $Re = 800$, 400, and 10^{-6} a secondary recirculation subcavity eventually forms, the geometries of both the dynamic and the final configurations differ drastically.

In the case of creeping (here $Re = 10^{-6}$) flow, an almost symmetry is developed and maintained, throughout the time evolution, about the center line of the cavity. In particular the corner eddy sizes are nearly equal. At near steady state (20×10^{-8} seconds in Fig. 22) the relative sizes of the primary and secondary vortices of the creeping flow agree with those obtained by Pan and Acrivos for linear Stokes flow in a cavity of the same aspect ratio.

It is of some interest to examine the relationship of low Reynolds number nonlinear flow to linear flow dynamics at various Reynolds numbers. A comparison of Fig. 23 for linear Stokes flow at $Re = 400$ with Fig. 22 for creeping nonlinear flow shows that the linear flow dynamics approximates the creeping flow dynamics very well, although in a much dilated time frame. Figure 24 shows for further comparison the results for linearized creeping flow of $Re = 10^{-6}$. Note the excellent correspondence between Fig. 22 and Fig. 24.

3.4. *Deep Cavity Flows*

With increasing depth, secondary corner eddy behavior should begin to exhibit features of highly viscous flows, due, in part, to the much lower velocity prevalent in the lower confines of the cavity. The upper region, where the characteristic velocity is $O(1)$, should preserve the features of the given global Reynolds number. These remarks are borne out by observing flow in cavities with $A > 2$. We restrict attention there to $A = 4.0$ although similar results were seen in the cases $A = 5.0$ and $A = 6.0$ that we ran.

A history of the normalized velocity field for the driven cavity having Reynolds number $Re = 400$ and aspect ratio $A = 4$ can be followed in Fig. 25. Salient features include the compartmentalization of the cavity into three separate regions of recirculation and the binary origin, due to fusing of the corner eddies, of all but the second down subregion of circulation. At 60 seconds the three subregions had formed, but a "final state is not achieved until 150 seconds. For a creeping flow case $Re = 10^{-6}$ at aspect ratio $A = 4.0$, see Fig. 26. For this case a "final" state was achieved at $t = 18 \times 10^{-8}$. These "final" states miss, of course, fine corner detail.

3.5. *Flow Dynamics at Higher Reynolds Numbers*

At the behest of one of the referees, we computed the flow dynamics at the higher Reynolds number $Re = 2000$. See Fig. 27. The vortex dynamics is similar to that at $Re = 400$ and $Re = 800$ although the tendency for the second primary vortex, once formed, to shift to the right is more pronounced. This causes the right corner secon-

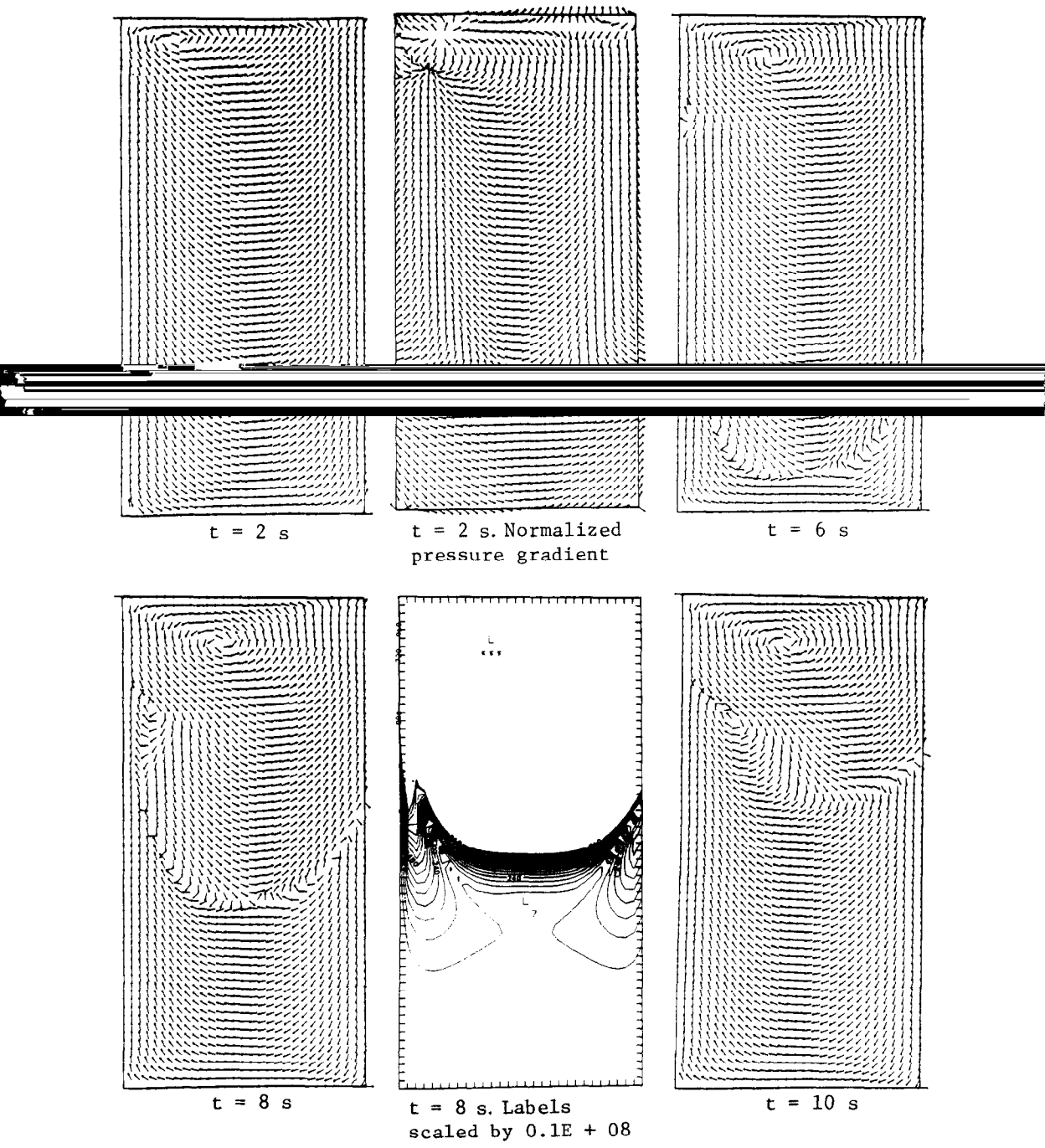

FIG. 25. Evolution of deep cavity flow ($A = 4.0$) of Reynolds number $Re = 400$. At 150 s the maximum norm between successive time steps of the velocity field, i.e., $\|V^n - V^{n-1}\|_\infty$, is $O(10^{-11})$.

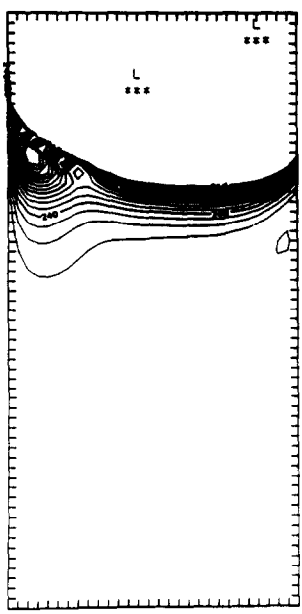

t = 10 s. Labels
scaled by 0.1E + 06

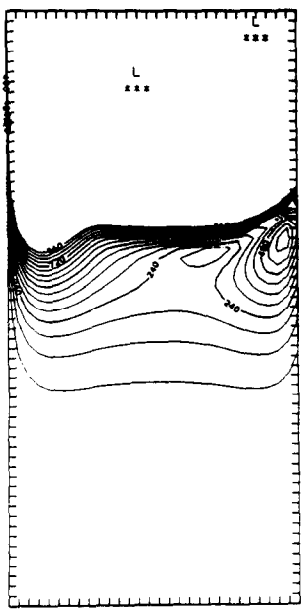

t = 10 s. Labels
scaled by 0.1E + 07

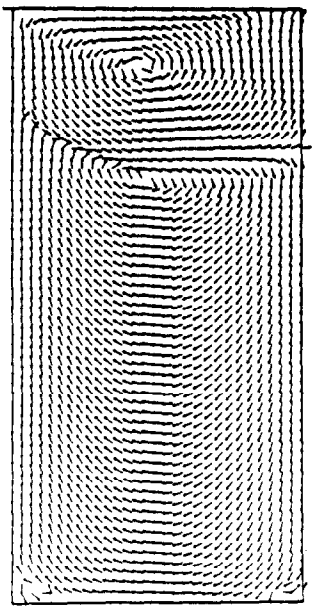

t = 16 s

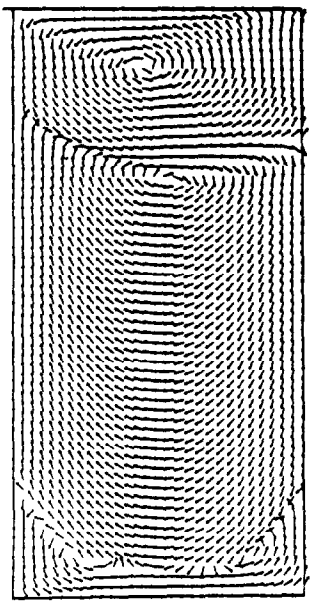

t = 20 s

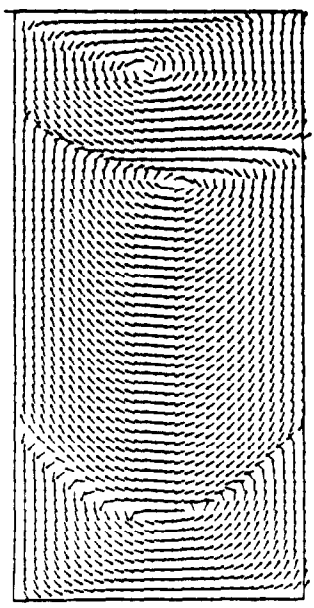

t = 24 s

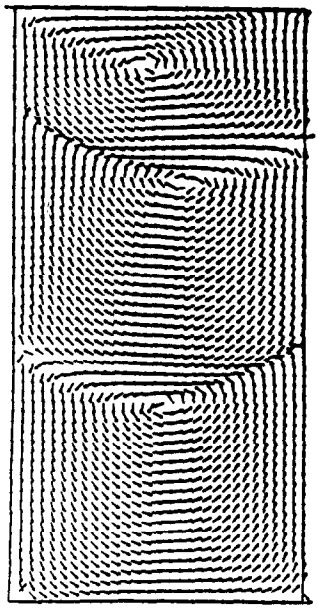

t = 40 s

FIG. 25—*Continued.*

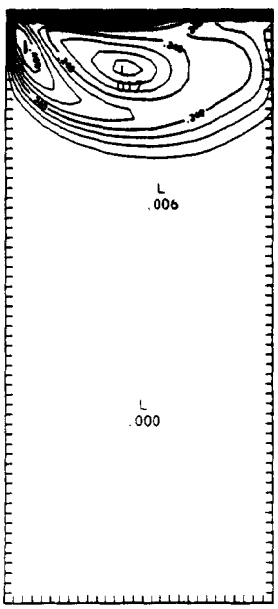

t = 40 s. Labels unscaled

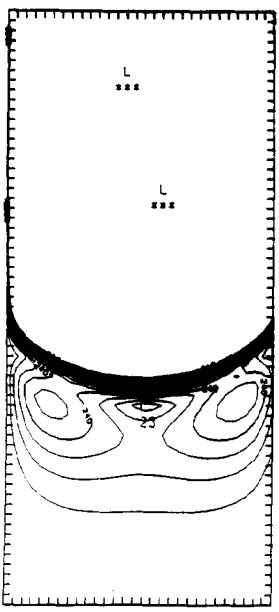

t = 40 s. Labels scaled by 0.1E + 08

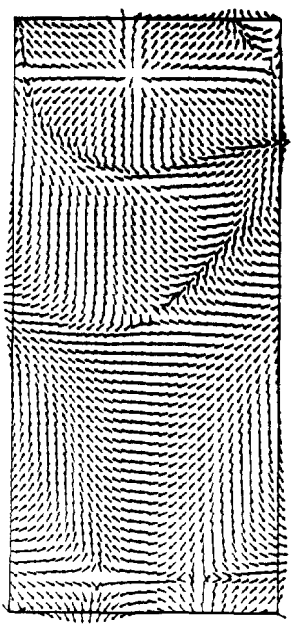

t = 40 s. Normalized pressure gradient

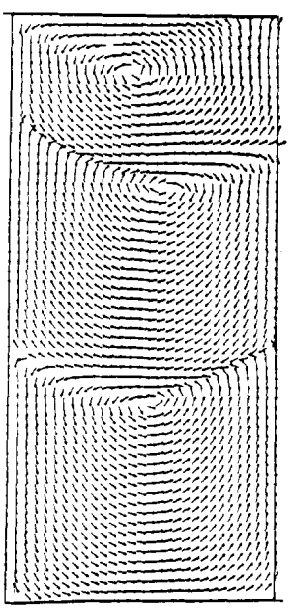

t = 42 s

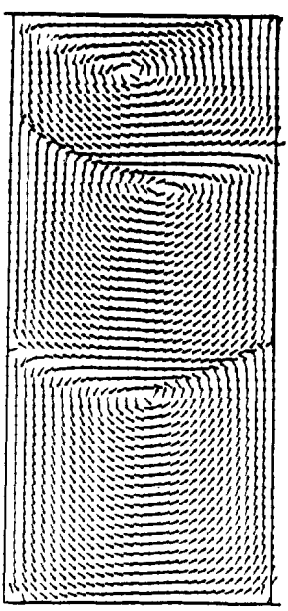

t = 48 s

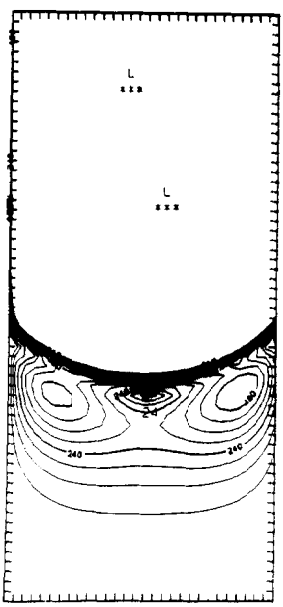

t = 48 s. Labels scaled by 0.1E + 08

FIG. 25—*Continued.*

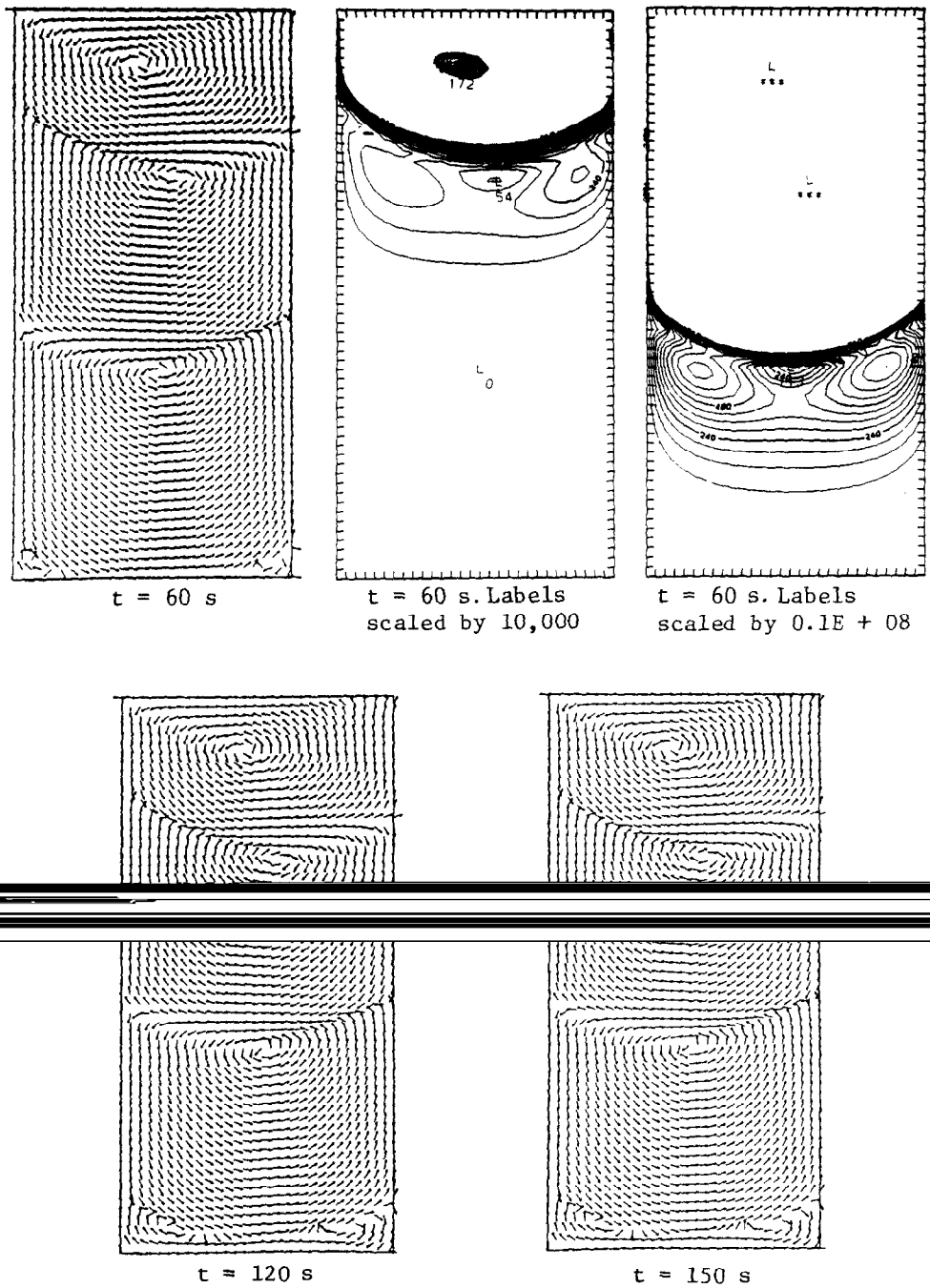

FIG. 25—*Continued.*

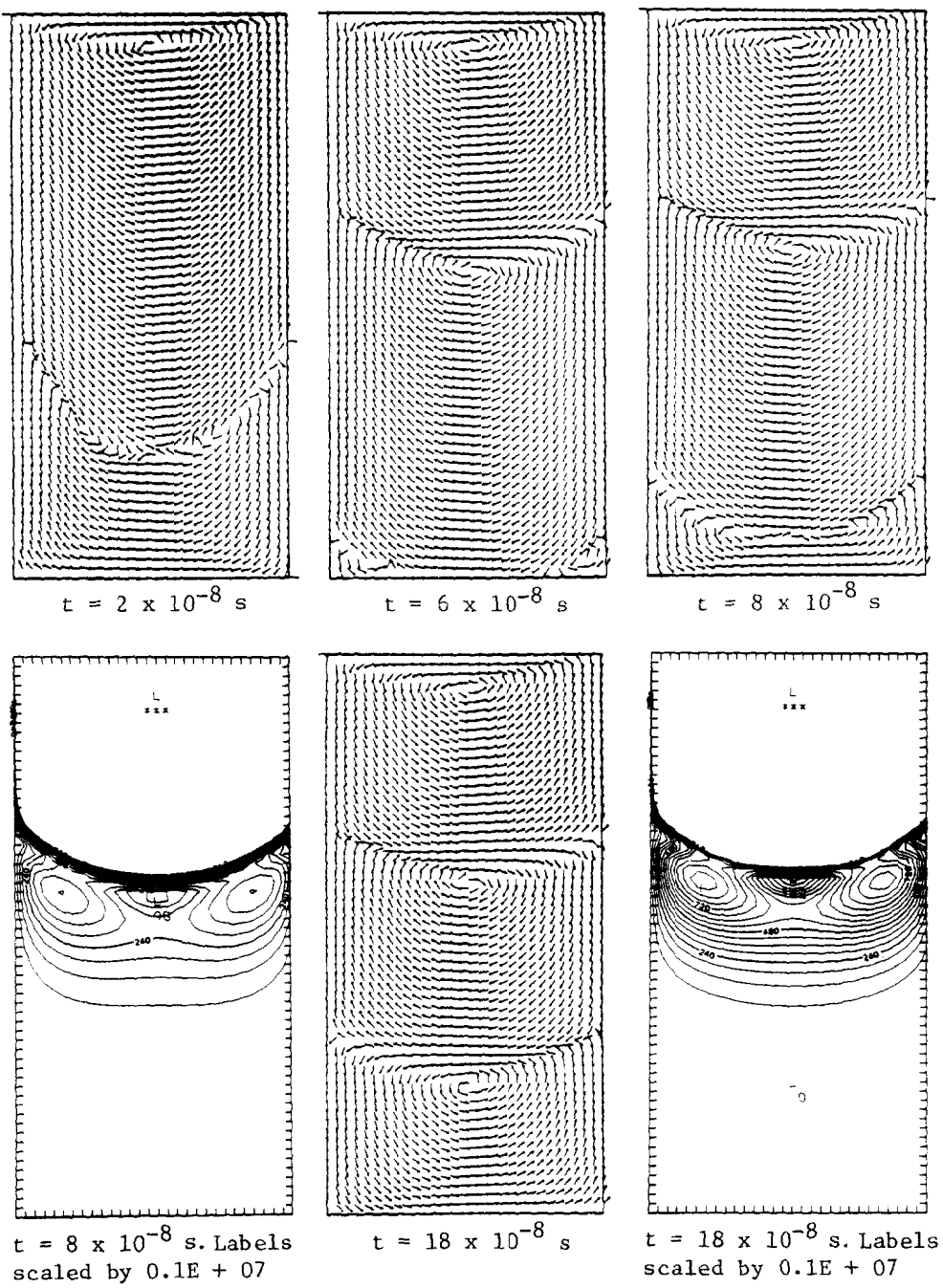

FIG. 26. Evolution of nonlinear Stokes flow ($Re = 10^{-6}$) within cavity of aspect ratio $A = 4.0$. At $T = 40 \times 10^{-8}$ seconds the maximum norm between successive time steps of the velocity field is $O(10^{-10})$.

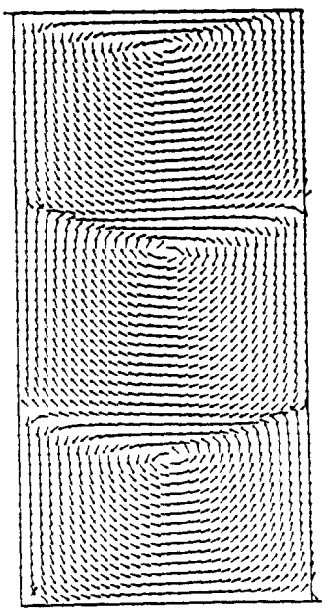

$t = 30 \times 10^{-8}$ s

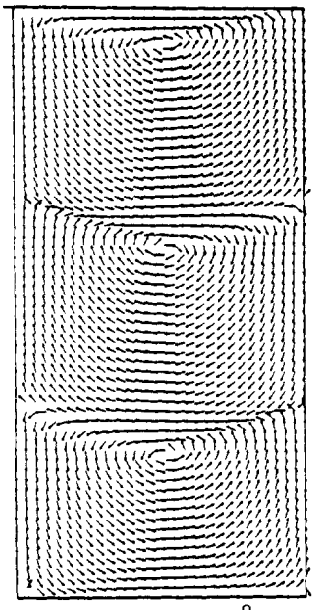

$t = 40 \times 10^{-8}$ s

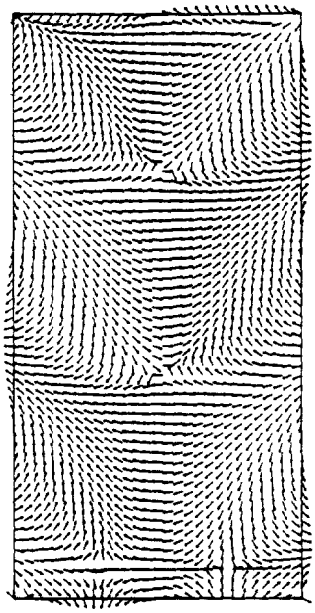

$t = 40 \times 10^{-8}$ s. Normalized pressure gradient

FIG. 26—*Continued.*

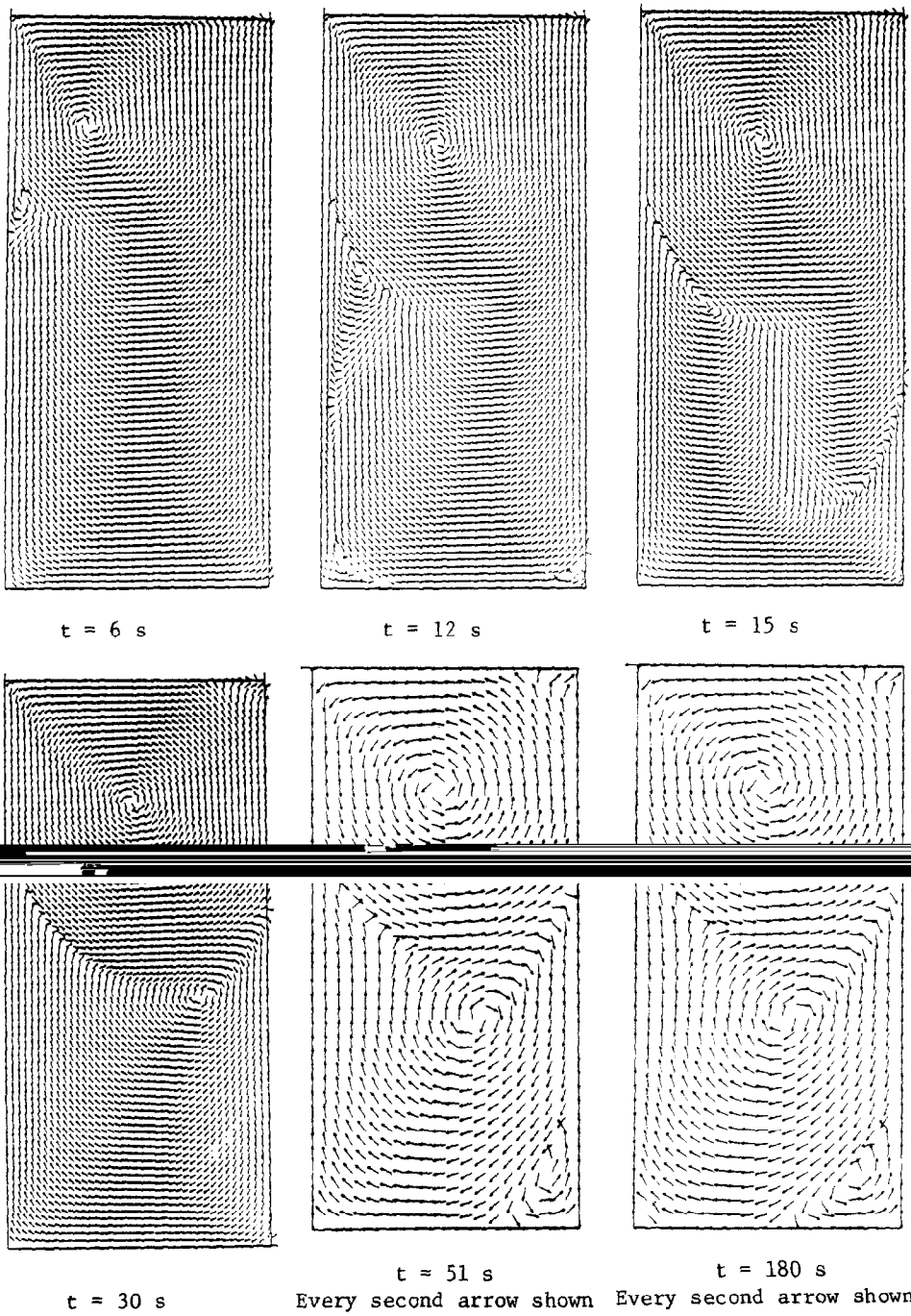

FIG. 27. Dynamics and final state of flow ($A = 2$) at Reynolds number $Re = 2000$. Time step $\Delta t = 0.003$, at 180 s $\|V^n - V^{n-1}\|_\infty$ is $O(10^{-7})$.

dary eddy to also be more pronounced. The use of suitably small time steps, e.g., $\Delta t = 0.003$ on a 40×80 grid, precluded any numerical instabilities. The trade-off between further reduction of the time step to accommodate both higher-resolution grids and larger Reynolds numbers would depend on machine resources available, and would eventually be limited by machine accuracy.

REFERENCES

1. R. AGARWAL, "Computation of Steady Recirculating Flows with a New Navier–Stokes Algorithm," McDonnell—Douglas Res. Lab. Report 84–20, 1984 (unpublished).
2. Y. Y. AZMY AND J. J. DORNING, "Nodal Integral Method Solutions and Singular Points for Driven Cavity Problems," *Numerical Methods in Laminar and Turbulent Flow*, C. Taylor *et al.* (Pineridge Press, Swansea, 1983), p. 582.
3. A. S. BENJAMIN AND V. E. DENNY, *J. Comput. Phys.* **33**, 340 (1979).
4. J. D. BOZEMAN AND C. DALTON *J. Comput. Phys.* **12**, 348 (1873).
5. O. BURGGRAF, *J. Fluid Mech.* **24**, 113 (1966).
6. T. B. GATSKI, C. E. GROSCH, AND M. E. ROSE, *J. Comput. Phys.* **48**, 1 (1982).
7. U. GHIA, K. N. GHIA, AND C. T. SHIN, *J. Comput. Phys.* **48**, 387 (1982).
8. P. GRESHO, R. LEE, AND R. SANI, "On the Time-Dependent Solution of the Incompressible Navier–Stokes Equations in Two and Three-Dimensions," *Recent Advances in Numerical Methods in Fluids*, edited by C. Taylor and K. Morgan (Pineridge Press, Swansea, 1980), p. 27.
9. K. GUSTAFSON AND K. HALASI, "Vorticity, Incompressibility, and Boundary Conditions in the Numerical Solution of the Navier–Stokes Equations," *Differential Equations*, edited by I. Knowles and R. Lewis (North-Holland, Amsterdam, 1984), p. 257.
10. K. GUSTAFSON AND K. HALASI, "On the Divergence-Free (i.e. Mass Conservation, Solenoidal) Condition in Computational Fluid Dynamics: How Important Is It?", *Numerical Methods in Laminar and Turbulent Flow*, edited by C. Taylor *et al.* (Pineridge Press, Swansea, 1983), p. 617.
11. K. GUSTAFSON AND R. LEBEN, *Appl. Math. Comput.* in press.
12. D. JEFFREY AND J. SHERWOOD, *J. Fluid Mech.* **96**, 315 (1980).
13. M. KAWAGUTI, *J. Phys. Soc. J.* **16**, 2307 (1961).
14. H. K. MOFFATT, *J. Fluid Mech.* **18**, 1 (1964).
15. F. PAN AND A. ACRIVOS, *J. Fluid Mech.* **28**, 643 (1967).
16. R. PEYRET AND T. D. TAYLOR, *Computational Methods for Fluid Flow* (Springer–Verlag, New York, 1983).
17. R. SCHREIBER AND H. B. KELLER, *J. Comput. Phys.* **49**, 165 (1983).
18. R. SCHREIBER AND H. B. KELLER, *J. Comput. Phys.* **49**, 310 (1983).
19. S. TANEDA, *J. Phys. Soc. J.* **46**, 1935 (1979).
20. F. THOMASSET, *Implementation of Finite Element Methods for Navier–Stokes Equations* (Springer–Verlag, New York, 1981).
21. M. VAN DYKE, *An Album of Fluid Dynamics* (Parabolic Press, Palo Alto, CA, 1982).